Arabian Journal of Chemistry (2022) **15**, 104252

King Saud University

**Arabian Journal of Chemistry**

www.ksu.edu.sa
www.sciencedirect.com

ORIGINAL ARTICLE

# Biomass valorization of walnut shell into biochar as a resource for electrochemical simultaneous detection of heavy metal ions in water and soil samples: Preparation, characterization, and applications

**Youssra El Hamdouni [a], Souad El Hajjaji [a], Tamás Szabó [b], László Trif [b], Ilona Felhősi [b], Khaoula Abbi [c], Najoua Labjar [c], Lina Harmouche [a], Abdul Shaban [b,*]**

[a] *Laboratory of Spectroscopy, Molecular Modeling, Materials, Nanomaterials, Water and Environment, Faculty of Sciences, CERNE2D, Faculty of Sciences, Mohammed V University in Rabat, Morocco*
[b] *Institute of Materials and Environmental Chemistry, Research Centre for Natural Sciences, Budapest, Hungary*
[c] *Laboratory of Spectroscopy, Molecular Modeling, Materials, Nanomaterials, Water and Environment, ENSET, CERNE2D, ENSAM, Mohammed V University in Rabat, Morocco*

Received 14 June 2022; accepted 8 September 2022
Available online 14 September 2022

**KEYWORDS**

Biochar;
Walnut shell;
Tyrosine film;
Heavy metal ions;
Carbon paste electrode;
Electrochemical detection

**Abstract** Lately, due to its accessibility and eco-friendliness, walnut shell biochar (WS-BC) is gaining attention as an electrode material component in the electrochemical detection of water pollutants. The overall performance of WS-BC is reliant on the nature of raw biomass and the production methods as well. In our concept, biochar, prepared from raw walnut shell (WS) by pyrolysis, was added to a carbon paste electrode (CPE), and poly-tyrosine (p-Tyr) was electrodeposited on the surface of the BC-doped electrode. The conditions of the elaboration of the electrode, such as pH, potential, and the number of deposition cycles, pH were optimized. The obtained p-Tyr-BC-CPE platform was tested for the determination of cadmium, lead, copper, and mercury ions in water and soil samples, using square wave voltammetry (SWV). The raw WS biomass and its BC were examined by thermal analysis (TG-DSC), X-ray diffraction (XRD), Fourier transform infrared spectroscopy (FTIR), and scanning electron microscopy coupled with energy-dispersive X-ray spectroscopy (SEM/EDX) techniques. The synergistic effects of the coexistence of the WS-BC and the

* Corresponding author.
E-mail address: shaban.abdul@ttk.hu (A. Shaban).
Peer review under responsibility of King Saud University.

Production and hosting by Elsevier

https://doi.org/10.1016/j.arabjc.2022.104252

**Nomenclature**

(WS) Walnut shell
(WS-BC) Walnut shell biochar
(CPE) Carbon paste electrode
(p-Tyr) Poly-tyrosine
(TG-DSC) Thermo-gravimetric analysis-differential scanning calorimetry
(XRD) X-ray diffraction
(FTIR) Fourier transform infrared spectroscopy
(SEM/EDX) Scanning electron microscopy coupled with energy-dispersive X-ray spectroscopy
(ICP-AES) Inductively coupled plasma-atomic emission spectroscopy
(ICP-MS) Inductively coupled plasma-mass spectrometry
(FAAS) Flame atomic absorption spectrometry
(GFAAS) Graphite furnace atomic absorption spectrometry
(CV) Cyclic voltammetry
(EIS) Electrochemical impedance spectroscopy
(SWV) Square wave voltammetry
(DOM) Dissolved organic matter

thin film of p-Tyr, for the detection of traces of heavy metal ions were investigated by electrochemical tests. The electrochemical characterization of the unmodified and modified electrodes was performed using the cyclic voltammetry (CV) and electrochemical impedance spectroscopy (EIS) methods, while the $Cd^{2+}$, $Pb^{2+}$, $Cu^{2+}$, and $Hg^{2+}$ detection experiments were studied using the CV and SWV techniques. The optimized experimental conditions for the p-Tyr-BC-CPE platform were evaluated. The obtained electrochemical results showed that the p-Tyr-BC-CPE platform produced excellent sensitivity toward the heavy metal ions: LOD of 0.086, 0.175, 0.246, and 0.383 nM for Cd(II), Pb(II), Cu(II) and Hg(II), respectively. The modified electrode platform displayed high selectivity, stability, and good reproducibility.



## 1. Introduction

Heavy metals (HM) are toxic pollutants, and although naturally occurring elements of our environment, they are also emitted from various artificial sources, such as automobiles, mining, fertilizers, tannery, battery, paper, and various other industries (Gumpu et al., 2015; Lim et al., 2018; Yadav et al., 2018). Heavy metal ions can persevere in the ecosystems for long periods and present severe risks to human and animal health and global biodiversity (Baig and Sajid, 2017). Some HM ions are essential ingredients to human metabolism, in very small quantities (like iron, copper, and zinc), but are harmful to their health in high doses (Mehta, et al., 2016). Other HM ions are toxic even at low doses (like lead, cadmium, and mercury) (He et al., 2005; Farzin et al., 2017).

When the toxic HM ions enter the food chain, they cause diseases such as lead poisoning (lead), nerve and kidney damage (mercury), bone damage (cadmium), and/or various cancer types of the bone marrow, kidneys, liver, or thyroid gland in humans (Rapini and Marrazza, 2017). Since the main cause of different forms of cancers was attributed to heavy metal ions poisoning, more attention and stricter regulations have been implemented to minimize the risks of HM ions accumulation in the environment (Lim et al., 2018). Currently, numerous conventional techniques have been applied for the detection and monitoring of heavy metal ions in water and wastewater, such as ICP-AES, ICP-MS, FAAS, GFAAS, and several electrochemical methods (Jlalia et al., 2021; Garciá-Miranda Ferrari et al., 2020).

Electrochemical techniques are acknowledged as significant in the fields of environmental analysis (Wang et al., 2021; Laghlimi et al., 2021), due to their economical cost, low running costs with low downtime, great efficiency, and excellent selectivity (Laghlimi et al., 2021). Carbon paste electrodes (CPEs) have been utilized wildly due to their easiness in restoration, steady response, and low ohmic resistance (Laghlimi et al., 2021; Smaini et al., 2019). Glassy carbon electrode (GCE) was also used as a useful tool as a detection platform in sensing (M. M. Foroughi., n.d.; Salajegheh et al., 2019). Electrode modification has been applied in analytical chemistry where several investigations were performed to quantify metal traces using modified carbon paste electrodes that have advantages such as simplicity, economical, non-toxic, and good selectivity (Smaini et al., 2019; Moutcine et al., 2020; Laghlimi et al., 2020).

Electrochemical sensors based on biochar (BC) materials are very promising due to their structure, physicochemical properties, and high sensitivity (Li et al., 2019; Wu et al., 2021). Several scholars focused on the production of biochar from agricultural waste materials. The produced biomass could increase the economic return and reduce contamination due to the high surface area, well-developed pore structure, rapid adsorption behavior, decent ion-exchange properties, and relatively easy regeneration process (Li et al., 2020; Zhang et al., 2019).

Amongst different agricultural-based adsorbents, the chemical composition of Walnut Shell (WS) displays great prospects as a sustainable source of active carbon for the remediation and extraction of toxic pollutants from water and soil environment. Walnuts are produced from a tree known as *Juglans regia* L, simply named walnut tree, which is commonly found in Asian European, and North African countries as well. Using raw biomass (WS) without additional alteration perhaps will not produce the anticipated results due to their restricted functionalities. For instance, WS biomass before activation has relatively low pore properties hindering its ability to reach full capacity in the adsorption process. Therefore, there is a progressively increasing number of studies in identifying new approaches to improve the physical and/or chemical characteristics of WS biochar (Albatrni et al., 2022).

The energy conversion of biomass is essentially based on thermal or hydrothermal conversion processes. Among these, pyrolysis is a rapidly developing technology with great potential for small-scale electricity production at a lower cost than any other possible biomass conversion (Albatrni et al., 2022). Consequently, thermochemical conversion procedures of WS biomass into biochar, such as pyrolysis in the absence of oxygen by conventional heating, are dominant to avoid secondary contamination. The obtained BC has a lowered H/

C and O/C ratio, though, depending on the duration and the temperature of pyrolysis, it preserves electron-rich groups, such as hydroxyl (OH), carboxyl (COOH), phenyl, and amino-functional groups (Ahmad et al., 2014). Certainly, the hydroxyl and carboxyl groups define the char's reactivity and constitute the possible binding sites for positively charged analytes i.e. heavy metal ions (Albatrni et al., 2022; Wu et al., 2018; Nguyen et al., 2019).

Recently, organic materials resulting from various agricultural side products have been used as precursors of biochars, such as sawdust (Madzaki et al., 2016), dates seeds (Chakraborty et al., 2019), olives seeds (Karakaş et al., 2016), corncobs (Lateef et al., 2019), rice husks, and straw (Vieira et al., 2020; Sharma et al., 2020), coffee beans waste (Zhang et al., 2020), hazelnut shell (Licursi et al., 2017), palm kernel shell (Bazargan et al., 2014); *Argania Spinosa* shells (Ifguis et al., 2022), coconut husks and walnut shell (WS) (Albatrni et al., 2022; Popoola, 2019), have all been used to prepare carbon materials.

Pyrolysis temperature selection is critical due to its effect on the alterations of the composition and structure, and a temperature increase decreases the biochar-derived dissolved organic matter (DOM) (Qiu et al., 2022; Bandara et al., 2020; Guo et al., 2022). Biochar can alter the species and distribution of HMs through adsorption–desorption, ion exchange, surface complexation, chemical mass precipitation, and reduction–oxidation reactions, thus decreasing the bioavailability of HMs and remediating HM contamination in water and soil, while also functioning as a soil enhancement agent (Qiu et al., 2022). However, the heavy metals removal and fixation efficiency in water and soils by biochar, is comparatively restricted. This disadvantage dictated the necessity for the surface modification of biochars as an appropriate technique to rise the removal efficiency of heavy metals. The immobilization of HMs takes place on the surface of biochar, and HMs may interact with dissolved substances in biochar as well. Water soluble substances in biochar include not only dissolved DOM, but also some water-soluble inorganic minerals (Bandara et al., 2020; Guo et al., 2022).

WS-BC can be modified, either physically or chemically, to enhance its applicability and adaptation for different environmental applications. Moreover, a polymer film of tyrosine can be introduced to the surfaces of the electrodes to enhance their sensitivity and stability by its good affinity for metal ions, giving place to new sensor platforms with desired and frequently preset qualities (Wang et al., 2021; Duan et al., 2017; Salih et al., 2017).

In the present contribution, WS biomass residues pose as sources for the production of BC. The physicochemical characteristics of the prepared BC were examined to inspect its potential application in a sensor platform for the detection of HM ions in aqueous solutions. The thermal properties, structure, and functional groups of the biochar were characterized through TG-DSC, XRD, FTIR, and SEM/EDX, respectively. The properties of the electrode, prepared with the contribution of BC, and a poly-tyrosine (p-Tyr) film on its surface, were investigated for the detection of $Cd^{2+}$, $Pb^{2+}$, $Cu^{2+}$, and $Hg^{2+}$ in water samples by CV, EIS, and SWV measurements under optimized conditions. The objective of this work is the development of a novel voltammetric sensor based on L-tyrosine film and walnut shell biochar to detect the trace of heavy metal ions in water and soil samples.

## 2. Materials and methods

### 2.1. Materials

The walnut shells were collected from the Marrakech-Safi Region (Morocco). Graphite powder was purchased from Lorraine ltd. L-tyrosine was purchased from Sigma-Aldrich. Nitrate salts of $Cd^{2+}$, $Pb^{2+}$, $Cu^{2+}$, $Hg^{2+}$, $Co^{2+}$, $Fe^{2+}$, $Mg^{2+}$, $Mn^{2+}$, $Ni^{2+}$, $Zn^{2+}$, and $Ca^{2+}$ were received from Merck. Hydrochloric acid, acetic acid, phosphoric acid, boric acid, sodium hydroxide, sodium acetate, dipotassium hydrogen phosphate, potassium dihydrogen phosphate, and potassium hexacyanoferrate were supplied by Fluka Chemika. All materials were analytical grade and used without any further purification treatment. All solutions were prepared with distilled water.

### 2.2. Preparation and characterization methods

#### 2.2.1. Preparation of walnut shells biochar

The walnut shells were selected, washed with deionized water to remove any impurities, dried at 105 °C for 24 hrs. to eliminate extra water, and then pulverized with a roller mill to obtain a product with 100–300 μm uniform particle size (Albatrni et al., 2022; Salih et al., 2017). The crushed product was pyrolyzed in a muffle furnace heated to 600 °C for 2 hrs. under vacuum. The obtained biochar was sealed in a hermetic vessel for further use.

#### 2.2.2. Preparation of real samples

For the practical tests of the sensor platform, soil and water samples were collected from *Bouregrag* River (Rabat-Sale Region). The soil samples were dried (at 105 °C for 24 h) and then pulverized with a crusher to obtain a soil powder of 50 μm sieve. For the extraction of HM ions, one gram of soil was mixed in 40 mL of acetate buffer solution ABS (0.10 M sodium acetate and acetic acid, pH 5.5), sonicated for 10 min., and then centrifuged for 15 min at 3500 rpm and finally filtered to obtain the soil extract solution. The river water sample was filtered (0.45 μm membrane) without any further pretreatment. Before the tests, the river water solution was diluted 2x with 0.10 M acetate buffer solution and adjusted the pH to 5.5. Finally, the soil and water samples were stored in a fridge at 4.0 °C for further use.

The standard solution containing 100 nM of $Cd^{2+}$, $Pb^{2+}$, $Cu^{2+}$, and $Hg^{2+}$ was applied to the samples and diluted to 0 nM of analytes. Then, concentrations of $Cd^{2+}$, $Pb^{2+}$, $Cu^{2+}$, and $Hg^{2+}$ in the soil and water samples were assessed by using the SWV technique with the same as above mentioned optimal conditions.

#### 2.2.3. Characterizations of walnut shells and biochar

The thermal behavior of the samples in the presence of an inert (99.999 % purity nitrogen) and oxidizing (99.999 % purity synthetic air) atmosphere was analyzed by a simultaneous thermo-gravimetric and differential scanning calorimetric analyzer (LabsysEvo, France). The measurements were performed in flowing (90 mL/min) gases, in alumina crucibles, in a 20–600 °C temperature range, with a heating rate of 10 °C/min. The obtained data were baseline corrected and further processed with the thermal analyzer's software (Calisto Processing, ver. 2.092). The thermal analyzer (both the temperature scale and calorimetric sensitivity) was calibrated by a multipoint calibration method, in which seven different certified reference materials were used to cover the thermal analyzer's entire operating temperature range.

The Walnut shell powder and its pyrolysis product were studied by XRD (Philips XPert Pro MPD). The Fourier transform infrared spectrometry was used to identify the functional groups that were present in the raw material and its pyrolysis product. FTIR measurements were recorded using Jasco FT/

IR-4600 apparatus (Tokyo, Japan), equipped with a Jasco-ATR-Pro-One single reflection diamond ATR accessory (incident angle 45°), and a DLATGS detector operating in the 4000–400 $cm^{-1}$ interval. A resolution of 4 $cm^{-1}$ and the co-addiction of 64 individual spectra were applied. Before the evaluation, an ATR correction (Jasco Spectra Manager v.2, Spectra analysis module version 2.15.11) was performed on the raw spectra. An SEM coupled with an EDX apparatus (FEI-Quanta 650) was used to scan the surface morphology and chemical composition of the walnut shell powder before and after pyrolysis.

### 2.3. Electrochemical measurements

The electrochemical measurements were performed using a potentiostat (SP-150-BioLogic science instruments) equipped with EC-Lab software. The three-electrode system configuration incorporated a carbon paste electrode (CPE) as the working electrode (WE), (A = 0.13 $cm^2$), a saturated calomel electrode (SCE) as the reference electrode (RE), and platinum wire as the counter electrode (CE). The working electrode was prepared by mixing the pyrolyzed walnut shells with graphite powder at 15 and 75 wt%, respectively, and paraffin oil. For comparison purposes, bare CPE was fabricated likewise without the addition of biochar (Dudek et al., 2018).

The poly-tyrosine-carbon paste (p-Tyr-CPE) and poly-tyrosine-biochar-carbon paste (p-Tyr-BC-CPE) electrodes were fabricated by electrochemical polymerization of the L-tyrosine monomer using the CV method. The electrochemical characterization of the unmodified and modified electrodes was done by utilizing the CV and EIS methods, while the $Cd^{2+}$, $Pb^{2+}$, $Cu^{2+}$, and $Hg^{2+}$ detection tests were studied using the SWV techniques. 40.0 mL of 0.1 M ABS was placed in the electrochemical cell having a predetermined concentration of the target heavy metal ions.

## 3. Results and discussion

### 3.1. Biochar structural, physical, and chemical properties

#### 3.1.1. Thermal measurements

The mass loss and heat flow (TG-DSC) curves of the walnut shell powder and its biochar, measured under $N_2$ and synthetic air atmosphere, from 20 to 600 °C, are shown in Fig. 1. It is observed that for the walnut shell product under oxidative (Fig. 1a) and inert conditions (Fig. 1b), small mass loss of 7 % (air) and 4 % ($N_2$) was observed up to 130 °C, accompanied by a small endotherm, due to the loss of physically bound water (moisture).

At temperatures from 200 °C to 500 °C in air, and 400 °C in nitrogen, the oxidative decomposition or pyrolysis of walnut shells occurs, i.e. the removal of chemically bound water, condensation of the remaining carbon content, volatilization of lighter compounds, and, in the case of air-treatment: oxidative burning. In both cases, the mass loss is separated into two steps around 350 °C (more characteristic in the presence of air), which is probably due to the structural inhomogeneity of the shell material, regarding the presence of both the less organized hemicellulose and the denser or more organized cellulose content. While at the end of the second step of mass loss, almost quantitative volatilization took place in the air, under inert conditions a much lower mass loss value was obtained, the rate of the mass loss decreased significantly above 400 °C, and slow pyrolytic degradation of the sample took place.

Regarding the energetics, under an oxidative atmosphere, overlapping exothermic peaks with peak maxima of 339 °C and 450 °C were found, which confirms that the decomposition and volatilization steps of the WS are accompanied by exothermic burning. Under inert conditions the shape of the heat flow profile is similar, but almost two orders of magnitude lower (Senneca et al., 2018; Xu et al., 2017), which points out that the pyrolyzed WS still contains some oxygen, which intramolecularly oxidizes carbon, leading to the appearance of the small overlapped exotherms.

Up to 500 °C, 97.45 % of the starting mass is lost in the air atmosphere, while under pyrolytic conditions ($N_2$ atmosphere) the corresponding mass loss was 71.97 %. In the case of the experiment performed in air, the remaining residue consisted of inorganic, mineral matter from the raw walnut shell powder, while in the case of the experiment performed in $N_2$, carbon was also present besides the above-mentioned inorganic matter.

From Fig. 1c, the mass loss of biochar in the oxidative atmosphere occurred in two stages: a slow mass loss of 15.40 % is visible up to 200 °C, due to the release of water, above this temperature, a second, large step can be seen, when almost all the carbon content was burnt to $CO_2$. In the case of the $N_2$ atmosphere (Fig. 1d), the biochar is generally stable in the whole temperature range with a weight loss of only about 10.40 %. The small weight loss could be resulting from the oxidative effect of the residual oxygen content (~10 ppm) in the nitrogen gas and/or from the intramolecular oxidation by oxygen-containing moieties in the sample. Based on this result, the raw walnut shells can be fully pyrolyzed at 600 °C.

#### 3.1.2. X-ray diffraction analysis

XRD was used to determine the eventual crystalline structure of the raw walnut shell and its biochar, as shown in Fig. 2. In the case of the raw walnut shell, two peaks were detected at a 2θ angle of around 18° and 22° assigned to a crystalline region of cellulose (Gupta et al., 2019). For the biochar, also two peaks are observed at 2θ values of around 23° and 43°, corresponding to (0 0 2) and (1 0 0) crystal planes of graphitic carbon (Salih et al., 2017; Janu et al., 2021). In the case of WS-BC (black curve in Fig. 2), the (0 0 2) diffraction peak located at around 22–26° (2θ) represented the layer spacing and thickness of the aromatic microcrystalline structure. The (1 0 0) diffraction peak at 42–45° (2θ) demonstrated that the microcrystalline structure changed from disorder to order under high-temperature pyrolysis.

The dispersion peak was not detected in XRD patterns, which demonstrated that the aliphatic chain in WS-BC was completely split. The parameters of lattice structure such as $d_{002}$ (inter-layer spacing), $L_c$ (crystallite height), and $L_\alpha$ (-crystallite diameter) were shown in Table 1. The value of $d_{002}$ - was 4.02, revealing that the inter-layer spacing of crystallite decreased and lattice arrangement was more ordered in biochars undergoing high-temperature pyrolysis. The values of $L_c$ and $L_\alpha$ were 0.07 and 0.144 nm, respectively. This could be explained by the increase in the size of crystallite, which

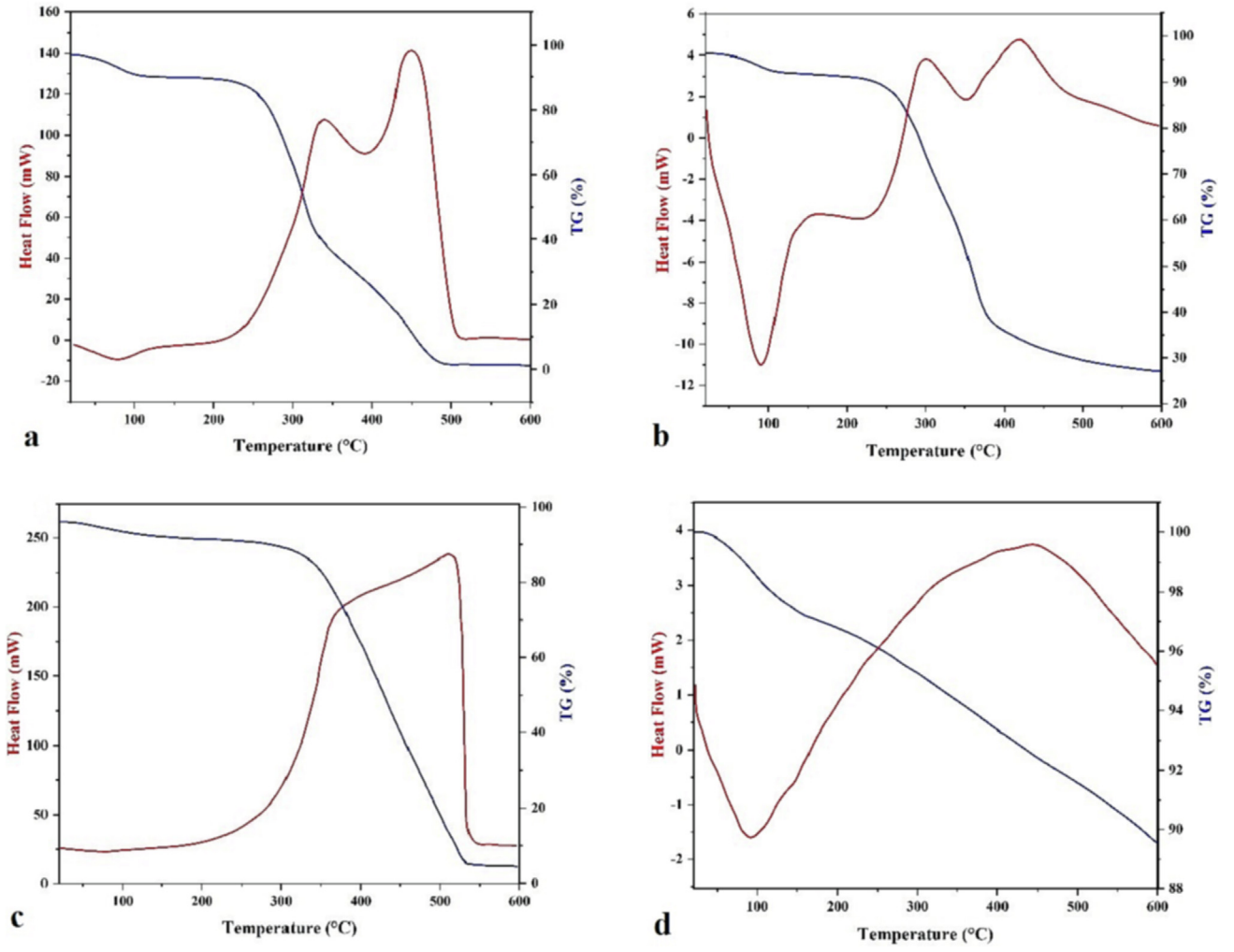


**Fig. 1** TG-DSC curves of the walnut shell powder (a - oxidative, b - pyrolytic) and its biochar (c - oxidative, d - pyrolytic).

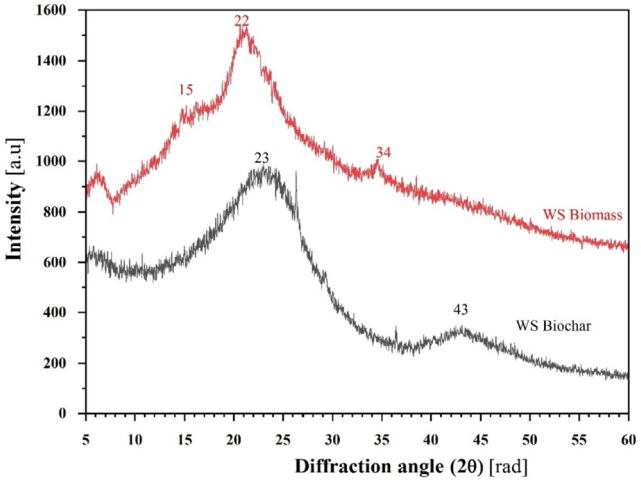


**Fig. 2** XRD characterization of raw WS biomass (red) and its biochar (black).

resulted in promoted graphite-like carbon structures in WS-BC. During the pyrolysis process, the crystallinity of the walnut shell reduces while its amorphous characteristics increase.

### *3.1.3. FTIR analysis*

To determine the presence of various functional groups on the WS biomass and its biochar, FT-IR spectroscopy was performed on the samples. The FTIR spectrum was measured in the range of 4000–400 $cm^{-1}$ with a resolution of 4 $cm^{-1}$ and the co-addiction of 64 individual spectra, as shown in Fig. 3. Major components of the WS biomass are hemicellulose, cellulose, and lignin. Lignin, unlike cellulose, possesses an olefinic carbon–carbon (-C═C-) double bond in cyclic as well as side chains and is aromatic (Yang and Qiu, 2010).

For the walnut shell, FTIR measurement records the intensive peaks at 3334 $cm^{-1}$ which corresponds to the υO-H stretching vibration (e.g. alcohols, phenols, and carboxylic acids); $\upsilon_{as}CH_2$ and $\upsilon_sCH_3$ stretching vibrations (2925 $cm^{-1}$) and $\upsilon_sCH_2$ and $\upsilon_sCH_3$ stretching vibrations (2850 $cm^{-1}$) of

**Table 1** The microcrystalline parameters of X-ray diffraction of WS and WS-biochars.

| Sample | $2\theta_{002}$(°) | $D_{002}$(nm) | $L_c$(nm) | $L_\alpha$(nm) | $2\theta_{001}$(°) | $B_{100}$(°) |
|---|---|---|---|---|---|---|
| raw WS | 21.4 | 4.02 | 0.07 | 0.144 | 35.2 | – |
| WS-BC | 23.3 | 3.7 | 0.09 | 0.19 | 43.4 | 8.5 |

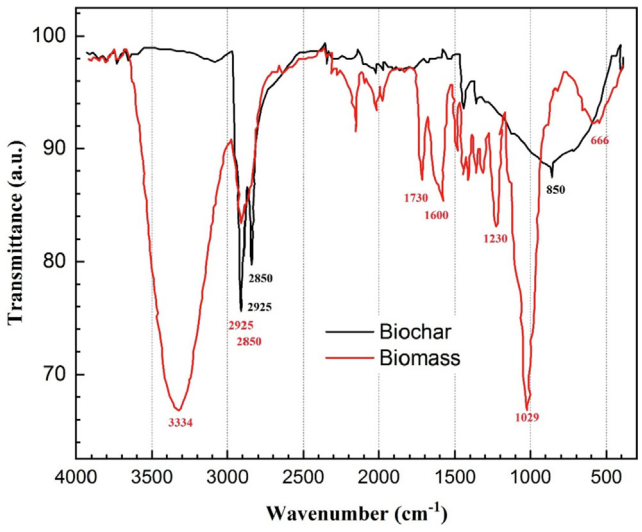


**Fig. 3** Identification of surface functional groups by FTIR spectra of the bare and walnut shell biochar.

methylene and methyl groups in the lignin structure; υC = O stretching vibration at 1730 $cm^{-1}$; $\upsilon_{as}$COO stretching vibration at 1600 $cm^{-1}$; υC–O (carboxylic and phenolic) and $\upsilon_{as}$C—O—C (ester) stretching vibration at 1230 $cm^{-1}$ and υC–O stretching vibration of primary –OH groups 1029 $cm^{-1}$. Lastly, the band assigned to the –OH out-of-plane bending vibrations band is located at 666 $cm^{-1}$ (Yang and Qiu, 2010; Lin et al., 2021).

The FTIR spectrum of the prepared walnut shell biochar is likewise shown in Fig. 3. All of the absorbance peaks corresponding to any 'O' content became removed or highly reduced after the pyrolysis processes applied at 600 °C for 2 h to the WS, due to the dehydration/dehydroxylation of the raw materials with the formation of water, and the release of light volatile matters. In the heating process. The BC spectrum reports that the alkane-related stretching vibrations (2925 $cm^{-1}$ and 2850 $cm^{-1}$), and the γC–H out of plane vibrations of C—H bonds attached to pillar atoms of C═C structures at 850 $cm^{-1}$ became dominant, as well as γC–H and γC–C deformation vibrations of di- and tri-substituted aromatic structures stand out of the background in the 1500–500 $cm^{-1}$ region.

A general note is that the FTIR study of biochar was carried out before mixing into the CPE and before it was modified with a −0.5 V - +2.0 V oxidative polymerization of tyrosine. Carbon-based electrodes can be easily oxidized with 0.0–2.0 V oxidative CV scanning (Li et al., 2019). This implies that after the fabrication of tyrosine not only a layer of p-Tyr but numerous –OH and –COOH groups were introduced onto the surface of the electrode.

### 3.1.4. Morphological study-SEM-EDX analysis

To examine the topography, morphology, and elemental composition SEM-EDX images of WS biomass and its corresponding biochar produced at 600 °C are shown in Fig. 4a, 4b, and 4c.

Fig. 4a shows that the surface of the walnut shell biomass is a completely fused structure with no visible pores at 10 and 100 μm resolutions. In Fig. 4b, the micrographs of the biochar morphology show the presence of voids and more porosity on its surface compared to that of the raw material. Comparing the SEM surfaces of the WS biomass and its WS-BC showed that the morphology became more complex because of aggregation and alteration of mineral compounds. Furthermore, due to the decomposition and volatilization of raw materials, a noticeable number of pores of different sizes (1.147 to 1.825 μm) appeared in WS-BC, as seen in Fig. 4b, at the resolution of 10 μm. This confirms that the produced WS-BC has a larger surface area than the raw WS biomass. This can be attributed to the fact that the heat treatment improves the porous structure of biochar due to the loss of the volatile matter in the walnut shell.

EDX analysis results are shown in Fig. 4c, where the results are presented in the mass percentage of the samples. Qualitative elemental composition analysis of raw walnut shell powder and its biochar using energy dispersive spectroscopy is listed in Table 2. According to Fig. 4c, carbon seemed to be the dominant element (43, 87 %), followed by oxygen (57, 11 %), for biomass and biochar, respectively. Traces of Ca (0.23, 0.94 %), and K (0.83 for the biomass), were also found in all biochars, but in very small amounts. The obtained results show that in the elemental composition of biochar a relatively high carbon content and much lower oxygen content whereas results for WS indicate that C (42.59 %) and O (56.97 %) while the values for the WS-BC are C (87.13 %) and O (11.09 %). Thus O/C ratio decreases from 1.34 to 0.13 with the pyrolysis of the walnut shell, indicating that pyrolysis is a suitable process for enriching carbon in biochar, due to dehydration-carbonization reactions at high temperatures (Xu et al., 2017).

## 3.2. Electrochemical characterization of the modified electrodes

### 3.2.1. Fabrication of the p-Tyr-BC-CPE modified electrode

The poly-tyrosine film was electrochemically deposited on the surface of BC-CPE using cyclic voltammetry from 2.0 mM L-tyrosine monomer dissolved in 0.2 M PBS at pH 7.0 in an electrochemical cell over the potential range of −0.6 V to 2.0 V at a scan rate of 100 $mV.s^{-1}$ for 20 successive cycles (Zbair et al., 2019). From Fig. 5, the first oxidation peak potential of the L-tyrosine monomer was observed at 1.01 V and the reduction peak appeared at −0.26 V. On continuous scanning, the anodic peak decreased gradually with the increase of the cycle number, indicating that the electro-polymerization of tyrosine was successful. The cathodic peak increased with the increase

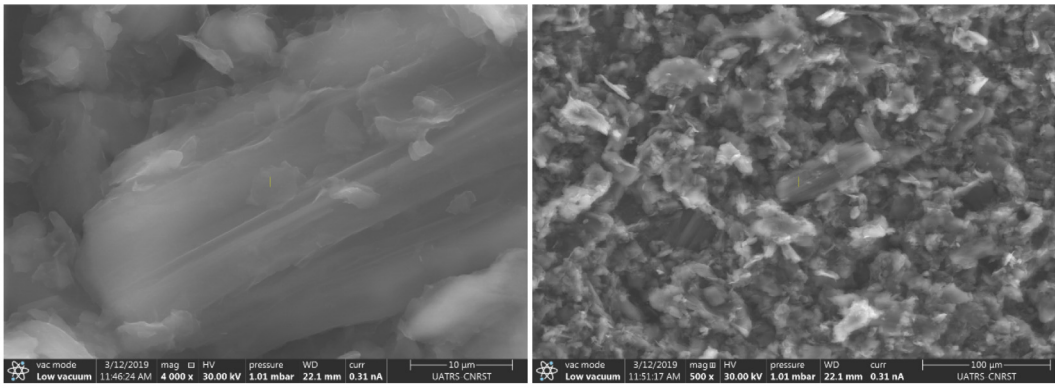

a. Images of Biomass at 10 and 100 µm resolution

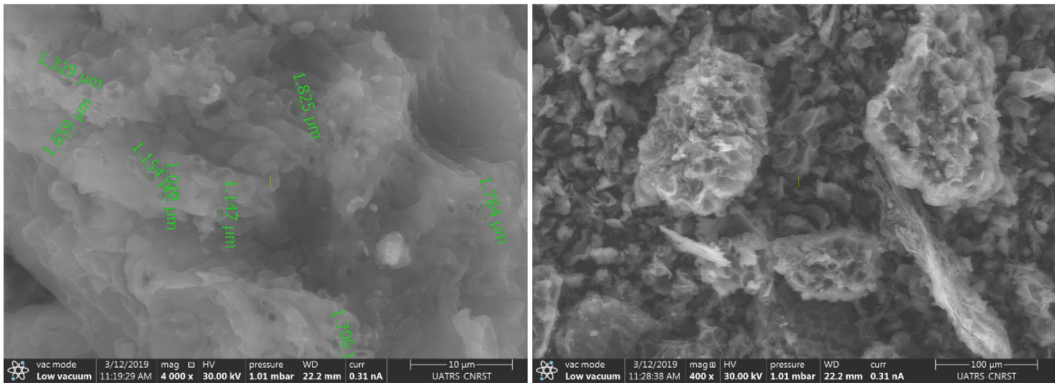

b. Images of Biochar at 10 and 100 µm resolution

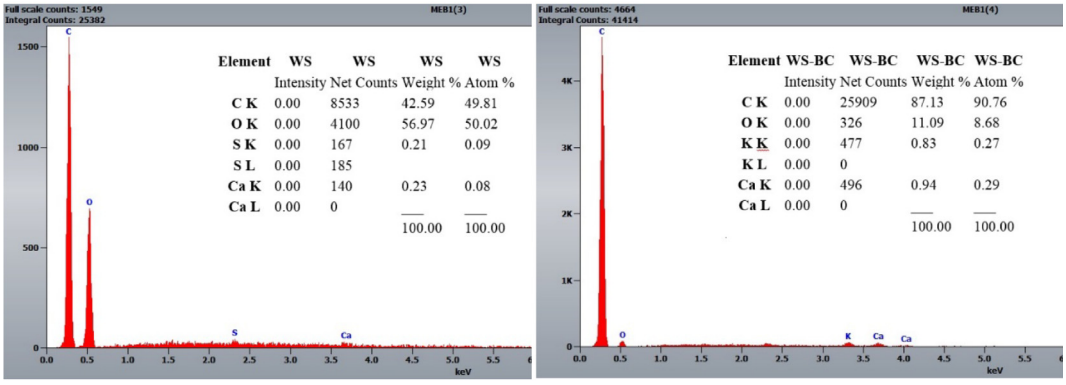


c. EDX images of WS-Biomass and WS-Biochar

**Fig. 4** SEM images of the walnut shell: Biomass (a), and the Biochar (b) at 10 and 100 µm resolution, EDX images of Biomass and Biochar (c), (green line indicates the pore diameter, see at 10 µm resolution).

**Table 2** Obtained elemental composition of walnut shell and its biochar at 600 °C.

| Samples | Elemental Composition (%) | | | | | |
|---|---|---|---|---|---|---|
| | C | N | O | K | Ca | O/C ratio |
| Walnut shell | 42.59 | 0.21 | 56.97 | – | 0.23 | 1.337 |
| Biochar | 87.13 | – | 11.09 | 0.83 | 0.94 | 0.127 |

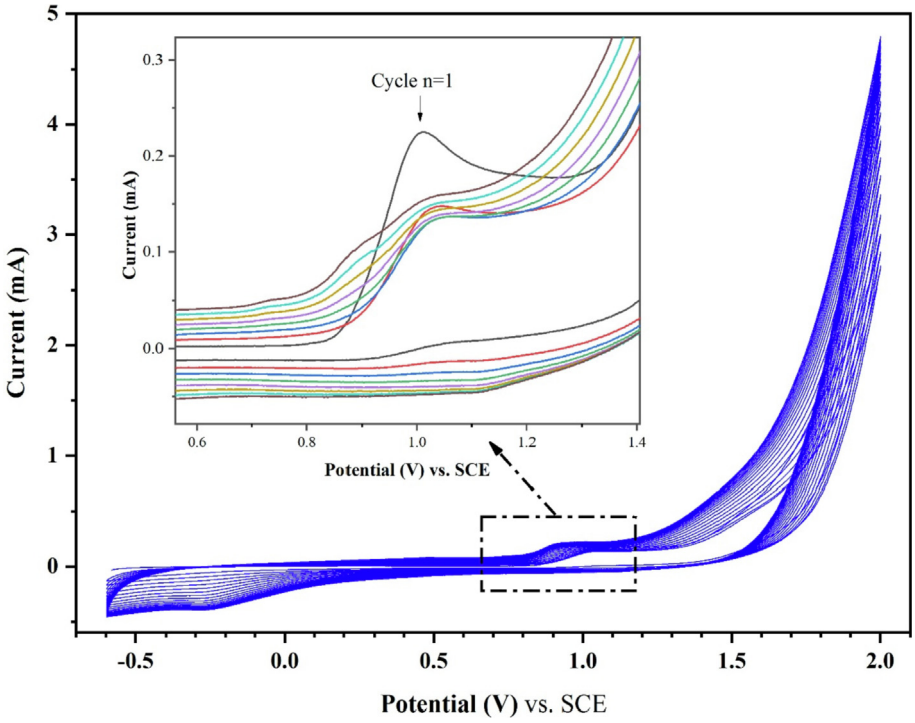


**Fig. 5** Cyclic voltammograms of p-Tyr-BC-CPE preparation in PBS (0.2 M, pH 7) containing 2.0 mM of Tyrosine at V = 100 mV.s$^{-1}$ from 1 to 20 cycles.

in cycling time, indicating that the poly-tyrosine film was growing on the modified electrode surface. After 20 cycles, a blank-blue film could be observed on the surface of BC-CPE, confirming the poly-tyrosine electrodeposition.

### *3.2.2. Electrochemical characterization of p-Tyr-BC-CPE*

The electrochemical properties of the modified electrodes were studied by CV and EIS using $[Fe(CN)_6]^{-3/-4}$ as a redox probe. Fig. 6a shows the CV responses of unmodified CPE and WS-CPE, BC-CPE, p-Tyr-CPE, and p-Tyr-BC-CPE modified electrodes in 1.0 mM $[Fe(CN)_6]^{-3/-4}$ electrolyte solution containing 5.0 mM KCl at a potential scan rate = 100 mV.s$^{-1}$. The bare CPE is characterized by a reversible redox reaction with a ΔE of 295 mV, indicating slow electron transfer on the CPE.

For the WS-CPE, the potential difference and the peak current show no significant difference between this response and that of CPE. This result is due to the poor conductivity of walnut shell biomass. After its modification with pyrolyzed biochar, the charge transfer was ameliorated, leading to a ΔE of 228 mV and a current increase to 0.064 μA, possibly due to the presence of the hydroxyl and carboxylic functional groups in the biochar surface, providing a large active surface and high adsorption capacity (Leftheriotis et al., 2007).

The p-Tyr-CPE showed significant improvement in redox behavior and current intensities. The potential difference ΔE observed is 95 mV. The intensity redox peaks are well defined and their intensity increased to 0.233 μA. These results indicate that the p-tyrosine film was successfully deposited on the electrode surface and can effectively promote electron transfer on the electrode surface (Wang et al., 2021).

The p-Tyr-BC-CPE showed a lower redox peak separation of 57 mV and a current increase to 0.556 μA. This is due to the synergetic effect between p-tyrosine film and biochar by increasing the electroactive surface area and improving the electrical properties of the electrode. It is important to note that p-Tyr-BC-CPE has much better conductive characteristics than p-Tyr-CPE and BC-CPE alone. This would indicate a serious synergistic effect between p-Tyr film and the BC additive, however, one should keep in mind that the CV polarization between −0.5 V and + 2.0 V can cause oxidative stress for the carbon materials, thus it cannot be excluded that the pyrolyzed biochar (with almost no O-content, due to IR report) suffered oxidation as well, and this might have contributed to the enhanced electro-activity of the p-Tyr-BC-CPE.

The electrochemically active surface area (A) of the electrodes was estimated using the Randles-Sevcik Eqs. (1) (Loaiza et al., 2011):

$$I_p = 2.69 \times 10^5 . n^{3/2} . A D^{1/2} . \upsilon^{1/2} . C \quad (1)$$

Where $I_p$, n, A, D, υ, and C represent the peak current, the number of electrons changed (n = 1), the electrochemical surface area of the electrode, the diffusion coefficient (7.60 × 10$^{-6}$ cm$^2$.s$^{-1}$), the scan rate, and the concentration of $K_3[Fe(CN)_6]$, respectively.

The electroactive surface areas for CPE, WS-CPE, BC-CPE, p-Tyr-CPE and p-Tyr-BC-CPE were 0.033, 0.060, 0.091, 0.33, and 0.75 mm$^2$, respectively. This shows that the p-Tyr-BC-CPE (A = 0.75 mm$^2$) had better electrochemical reactivity and, as such, was provided for simultaneous detection of $Cd^{2+}$, $Pb^{2+}$, $Cu^{2+}$, and $Hg^{2+}$.

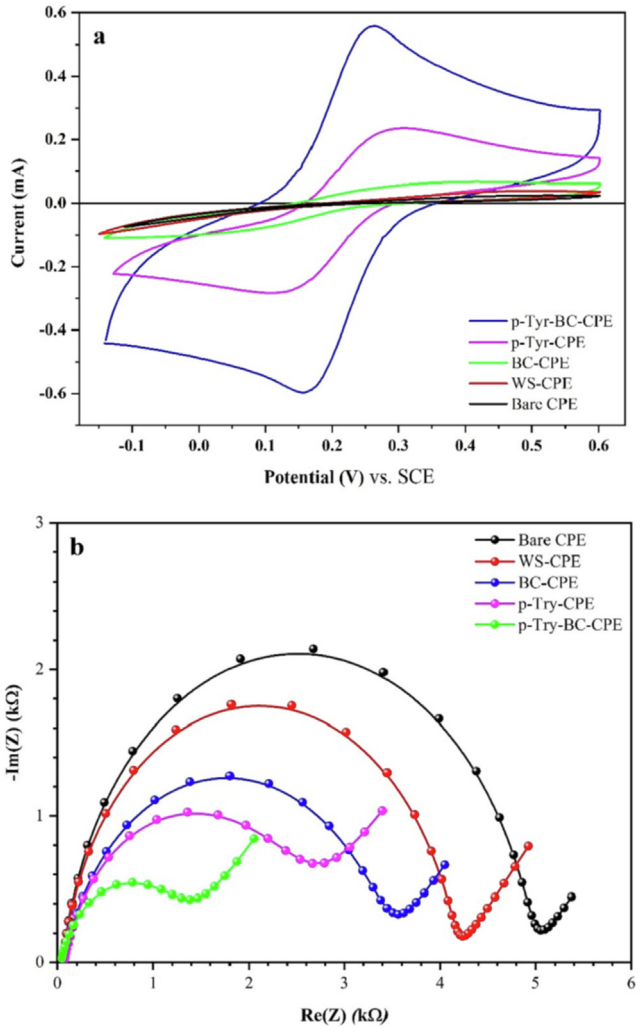


**Fig. 6** CV voltammograms (a) and EIS Nyquist plot (b) for bare CPE, and WS-CPE, BC- CPE, p-Tyr-CPE, p-Tyr-BC-CPE coated electrodes in 1.0 mM $[Fe(CN)_6]^{3-/4-}$ containing 0.5 mM KCl.

Electrochemical impedance spectroscopy (EIS) is applied to investigate the charge transfer processes on the surfaces of different coated electrodes. The impedance responses of unmodified and modified electrodes, measured at a 0.35 V bias potential (open circuit potential (OCP)) and frequency range from $10^{-1}$ to 105 Hz, were registered. EIS Nyquist plots for bare CPE, and WS-CPE, BC-CPE, p-Tyr-CPE, and p-Tyr-BC-CPE coated electrodes in 1.0 mM $[Fe(CN)6]^{3-/4-}$ containing 0.5 mM KCl, are represented in Fig. 6b. The resulting impedance diagrams are composed of a semicircle part at the high-frequency range, characterized by the parallel connection of the charge transfer resistance ($R_{ct}$) and double-layer capacitance ($C_{dl}$), while the linear part at low frequencies is related to the Warburg-diffusion process (Xiong et al., 2021). The Nyquist diagrams data were fitted by the standard Randle's equivalent circuit, having a chi-squared coefficient of $10^{-3}$.

The solution resistance ($R_s$) is determined by the conductivity of the electrolyte (which is determined by its composition) and the distance between the working electrode and the reference electrode. Both are specific to the conditions of the measurement, not to the tested system. The main parameters of the standard Randle's equivalent circuit affected by different coatings are the charge-transfer resistance ($R_{ct}$) and double layer capacitance ($C_{dl}$) as shown in Table 3. The $R_{ct}$ values of the bare CPE and the WS-CPE, BC-CPE, p-Tyr-CPE, and p-Try-BC-CPE coated electrodes, are tabulated in Table 3. The $R_{ct}$ value of the bare CPE electrode was obtained to be 613.0 $\Omega.cm^2$. The $R_{ct}$ values of WS-CPE and BC-CPE electrodes were lower, 511.7 $\Omega.cm^2$ and 417.7 $\Omega.cm^2$, respectively. The lower charge transfer resistance of modified electrodes is most probably the result of the increase of the effective surface area and the presence of surface active functional groups in the biomass layer. A much more significant decrease of $R_{ct}$ was obtained for poly-tyrosine modified electrodes: 309 $\Omega.cm^2$ for p-Tyr-CPE, and 158.8 $\Omega.cm^2$ for p-Tyr-BC-CPE. This means of 50 % decrease in the case of p-Tyr-CPE compared to bare CPE and a 62 % decrease in the case of p-Tyr-BC-CPE compared to BC-CPE electrodes.

The $R_p$ decrease is related to the presence of p-Tyr-biochar which could effectively accelerate the electron transfer, which is consistent with the CV results. The double-layer capacitance values characterize the interfacial properties of electrodes. There was only a minor difference obtained between $C_{dl}$ of bare CPE and WS-CPE electrodes, 4.9 $\mu F.cm^{-2}$ and 5.3 $\mu F.cm^{-2}$, respectively, because of the similar surface condition (Table 3). The BC-modified CPE electrode has increased $C_{dl}$ (19.1 $\mu F.cm^{-2}$), which points out the presence of surface-active functional groups in the porous BC-layer. A much larger increase in $C_{dl}$ is attained with p-Tyr-modified electrodes, 993 $\mu F.cm^{-2}$ for p-Tyr-CPE and 1817 $\mu F.cm^{-2}$ for p-Tyr-BC-CPE electrodes. This significant increase in the double layer capacitance can be attributed to various reasons, including the increase in the effective surface area and the presence of surface active functional groups in the thick porous layers.

### 3.2.3. *Effect of scan rate on the sensor efficiency*

To determine the electrochemical mechanism of the $Fe^{2+}/Fe^{3+}$ redox process on the prepared p-Tyr-BC-CPE, the influence of scan rate variation was investigated. Fig. 7a shows

**Table 3** Variation of the solution and polarization resistances in the Randles standard equivalent circuit for different sensor platforms.

| Sensor Platform | Solution resistance ($R_s$) [$\Omega.cm^2$] | Polarization resistance ($R_{ct}$) [$\Omega.cm^2$] | Double-layer capacity ($Q_{dl}$)[$\mu F.cm^{-2}$] |
|---|---|---|---|
| Bare CPE | 10.2 | 613.0 | 4.88 |
| WS-CPE | 10.2 | 511.7 | 5.31 |
| BC-CPE | 10.3 | 417.7 | 19.15 |
| p-Tyr-CPE | 11.4 | 309.0 | 992.8 |
| p-Try-BC-CPE | 6.5 | 158.8 | 1817.0 |

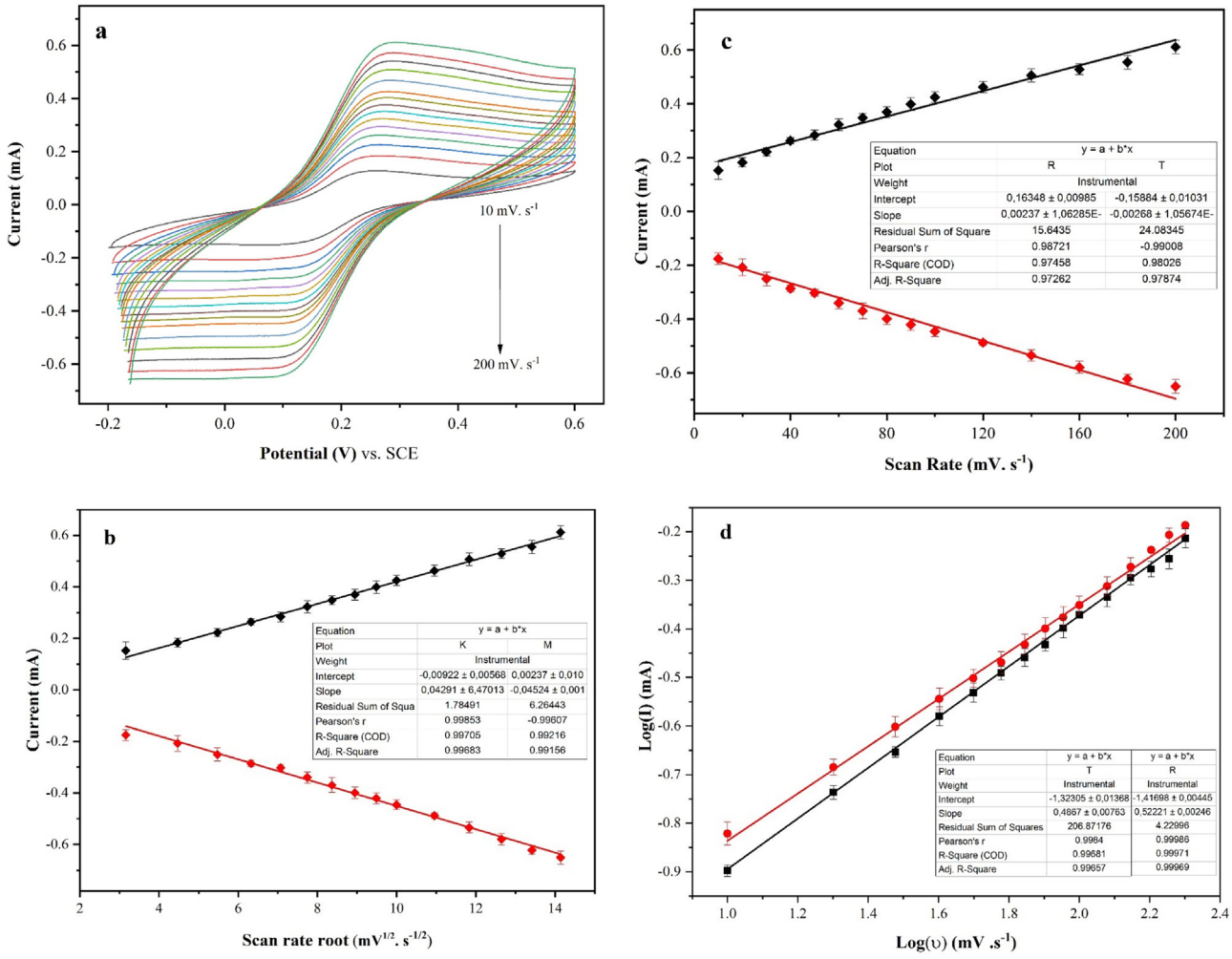


**Fig. 7** Scan rate effect of the modified electrode from 10 to 200 mV.s$^{-1}$ (a), the effect of the variation of $\upsilon^{1/2}$ on the redox current intensity (b), the effect of the variation of $\upsilon$ on the redox current intensity (c), and the effect of the variation of Log($\upsilon$) on log(I) (d) (potentials are referred to SCE).

the CV measurements in 1.0 mM of $[Fe(CN)_6]^{3-/4-}$ at sweep rates ranging from 10 to 200 mV.s$^{-1}$. The results show a linear relationship between the redox peak currents and the square root of the scan rate ($\upsilon^{1/2}$), possibly indicating that the reaction process was controlled by diffusion (Yang et al., 2014; Pamuk et al., 2013). The relationship between the redox peak currents and ($\upsilon^{1/2}$), the dependence between the redox peak currents and the scan rate ($\upsilon$), and the relationship between the logarithm of the redox peak currents and the logarithm of the scan rates (log($\upsilon$)) are all linear as shown by Fig. 7b, 7c, and 7d, respectively.

Based on the literature review, when the slope of the logarithm of peak current versus the logarithm of scan rate has a value between 0.5 and 1.0, that means the detection mechanism is diffusion/adsorption controlled. As shown in Fig. 7d, the slope was 0.55 which is categorized as a mixed diffusion-adsorption controlled mechanism (Wang et al., 2011).

## 4. Optimization of the experimental conditions

To optimize the sensitivity of p-Tyr-BC-CPE for simultaneous detection of $Cd^{2+}$, $Pb^{2+}$, $Cu^{2+}$, and $Hg^{2+}$, several experimental conditions such as supporting electrolytes, pH values, deposition potentials, and deposition times, were investigated and the analytical performance was compared.

### *4.1. Optimization of the supporting electrolyte*

The supporting electrolyte has an important effect on the simultaneous detection of heavy metals. The test medium of HCl, phosphate, acetate, and Britton-Robinson buffer solution was measured in a solution containing 0.1 mM of $Cd^{2+}$, $Pb^{2+}$, $Cu^{2+}$, and $Hg^{2+}$ (Fig. 8a). The best height responses and well-defined peaks were obtained for all four target metal ions in acetate buffer solution due to its high electronic conductivity and good stability (Tesfaye et al., 2021). Thus, an ABS (0.1 M) was selected as the best electrolyte in further experiments.

### *4.2. Optimization of the electrolyte pH*

Additionally, the influence of pH values on the voltammetric response was also evaluated using ABS in a pH range from 3 to 6 (namely pH 3.0, 3.5, 4.0, 4.5, 5.0, 5.5, or 6.0) as shown

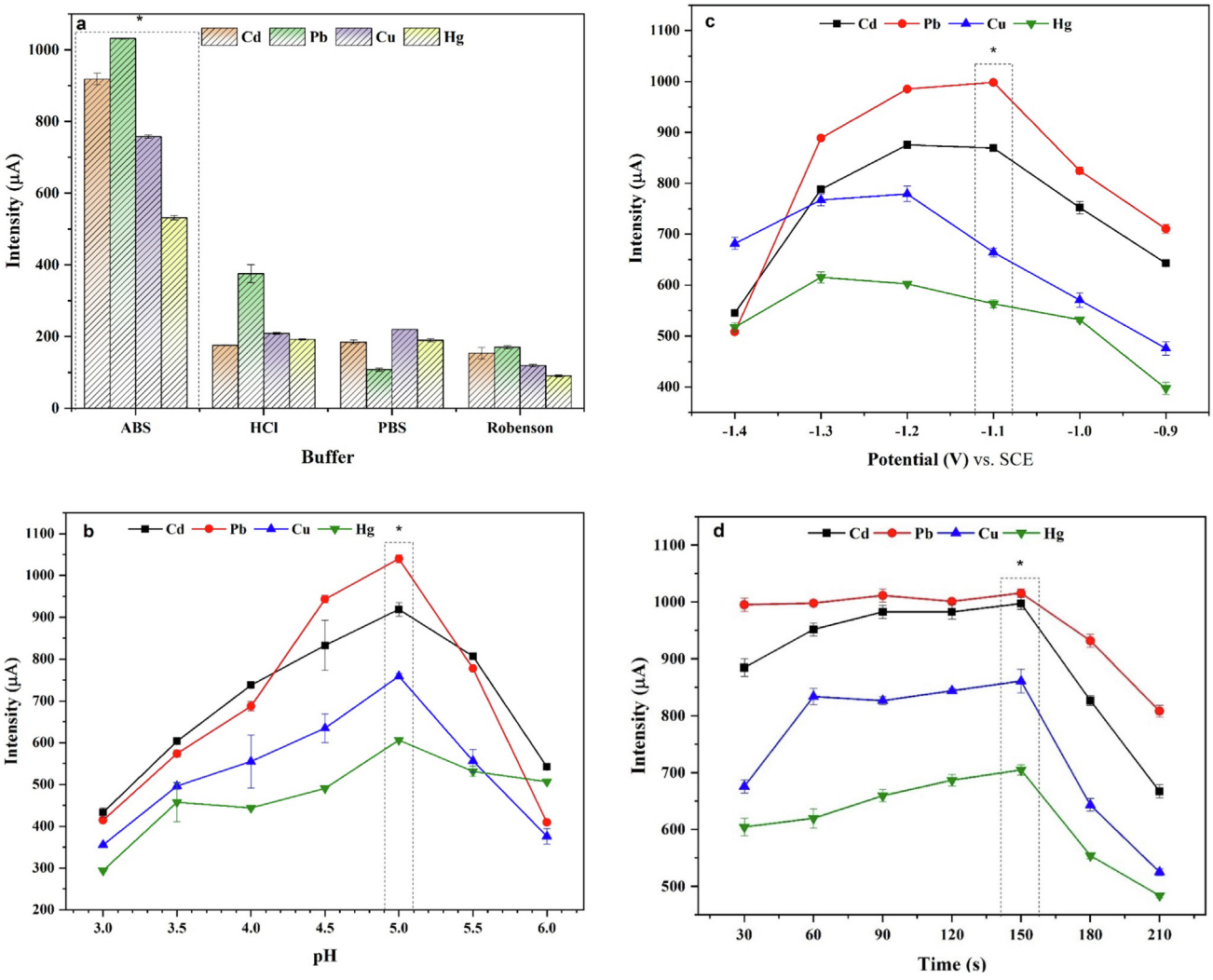


**Fig. 8** Experimental parameters effect (a) supporting electrolyte, (b) pH value, (c) deposition potential (potentials are referred to as the SCE)., (d) deposition time recorded in the p-Tyr-BC-CPE in the presence of 0.1 mM Cd(II), Pb(II), Cu(II), and Hg(II).

in Fig. 8b. The results indicated that the peaks currents for $Cd^{2+}$, $Pb^{2+}$, $Cu^{2+}$, and $Hg^{2+}$ increased when the pH was increased from 3 to 5 can be due to the competition between metallic ions and protons to binding sites on the electrode surface (Shivappa Adarakatti et al., 2017). The highest current peak was obtained at pH 5.0, possibly because of the better interaction between the modified electrode and target ions. At a higher pH value (5.0–6.0), the current intensity decreased due to the possibility of the formation of complexes between the hydroxyl ions of the electrolyte and heavy metal ions. Thus, a pH of 5.0 was chosen for further studies.

### *4.3. Optimization of the deposition potential*

The influence of the deposition potential on the metals stripping currents was investigated over the potential range from −1.4 to −0.9 V. As shown in Fig. 8c, the stripping peak currents increased when the deposition potential was decreased from −0.9 to −1.1 V, where Pb reached its maximum stripping value, while Cd and Cu peaked at −1.2 V, and Hg had its maximum at −1.3 V. At more negative deposition potentials all the respective stripping signals decreased. In other words, the −1.1 V potential is optimal for $Cd^{2+}$ and $Pb^{2+}$, whereas the −1.2 V potential is optimal for $Cu^{2+}$ and $Hg^{2+}$ but with some signal noise. This result could be assigned to the competitive generation of hydrogen present in the electrolyte solution (de Oliveira et al., 2017). Therefore, to minimize the effect of hydrogen generation, −1.1 V was chosen as accumulation potential.

### *4.4. Optimization of the deposition time*

The effect of deposition time was also studied in a range from 10 to 300 s (Fig. 8d). In the literature, the notion of saturation of the working electrode remains relevant even for heavy metals (especially when the detection mechanism is controlled by adsorption and diffusion processes) (Guo et al., 2017). The peak currents increased with the accumulation time. The peaking of the stripping signal in 150 s indicated that the electrode surface reached its maximum loading capacity. Elongated deposition time results in loss of stripping current intensities,

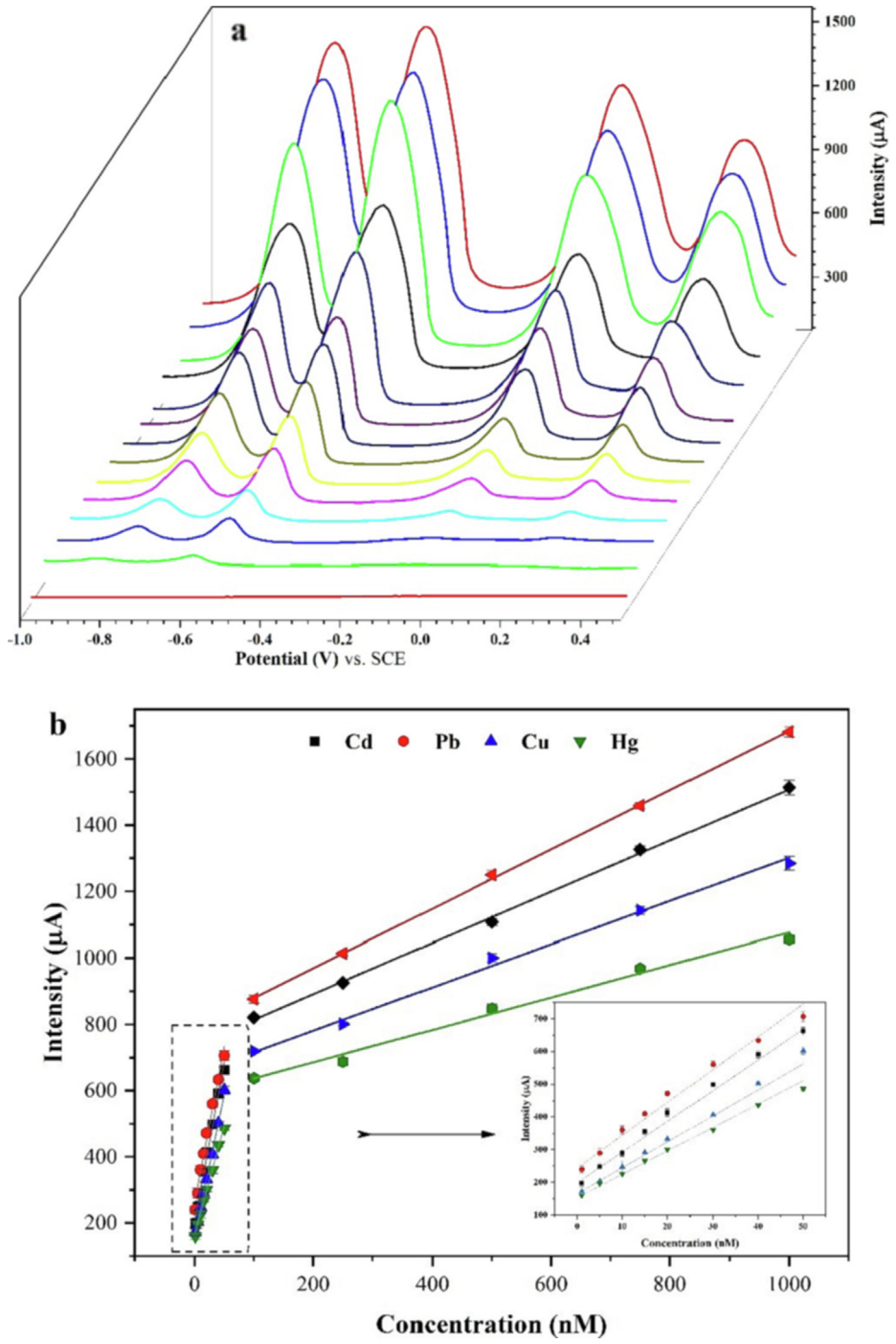


**Fig. 9** SWV voltammograms (a) and calibration curves (b) of the p-Tyr-BC-CPE for various concentrations of Cd(II), Pb(II), Cu(II), and Hg(II), (potentials are referred to as the SCE).

which suggests that, during accumulation, there is an equilibrium between two reactions: the increase and the decrease of the metal decorated electrode area. This phenomenon could be explained through the porous structure of the electrode. Firstly, the surface of the pores is covered with deposited metal (increasing stripping signal), and then secondly the pores get filled up, giving a flatter electrode surface (decreasing stripping signal) (Guo et al., 2017). Therefore, the deposition time was chosen as 150 s to obtain the optimal sensitivity for simultaneous detection of $Cd^{2+}$, $Pb^{2+}$, $Cu^{2+}$, and $Hg^{2+}$.

## 5. Characterization of the p-Tyr-BC-CPE electrode

### *5.1. Simultaneous detection of $Cd^{2+}$, $Pb^{2+}$, $Cu^{2+}$, and $Hg^{2+}$*

The p-Tyr-BC-CPE was applied for the simultaneous detection of $Cd^{2+}$, $Pb^{2+}$, $Cu^{2+}$, and $Hg^{2+}$ at different concentrations using SWV. Under the optimized experimental conditions, the stripping peak currents decrease simultaneously with the concentration of target HMs changing from 1 to 1000 nmol/

**Table 4** Regression equations and the calibration curve parameters.

| Metals | Conc. Range (nM) | Regression Equation | $R^2$ Value |
|---|---|---|---|
| Cd(II) | 1.0–75.0 | $I_p$ = 0.7199 [$Cd^{2+}$] + 757.5484 | 0.9992 |
| | 100–1000 | $I_p$ = 10.1329 [$Cd^{2+}$] + 189.5054 | 0.9943 |
| Pb(II) | 1.0–75.0 | $I_p$ = 0.8398 [$Pb^{2+}$] + 793.4105 | 0.9973 |
| | 100–1000 | $I_p$ = 11.3863 [$Pb^{2+}$] + 204.545 | 0.9819 |
| Cu(II) | 5–75 | $I_p$ = 0.6519 [$Cu^{2+}$] + 687.8306 | 0.9616 |
| | 100–1000 | $I_p$ = 8.7154 [$Cu^{2+}$] + 159.8240 | 0.9959 |
| Hg(II) | 5.0–75.0 | $I_p$ = 0.4788 [$Hg^{2+}$] + 571.6376 | 0.9597 |
| | 100–1000 | $I_p$ = 6.6023 [$Hg^{2+}$] + 168.3001 | 0.9815 |

**Table 5** Statistical properties of p-Tyr-BC-CPE.

| Metal ions | DL (nM) | DQ (nM) | RSD (%) |
|---|---|---|---|
| Cd(II) | 0.0861 | 0.2868 | 0.9896 |
| Pb(II) | 0.1754 | 0.5845 | 1.5949 |
| Cu(II) | 0.2463 | 0.8209 | 3.0943 |
| Hg(II) | 0.3834 | 1.2781 | 3.6931 |

L (Fig. 9a). Linear calibration curves were obtained in two linear dynamic ranges as indicated in Fig. 9b, and the regression equations as shown in Table 4. The evaluation techniques for the limit of detection (LOD) and the limit of quantification (LOQ) are similar except for the acceptable values of the constant numbers used in the determination using the standard deviation (σ) and linear range's slope (S): LOD = 3.3 * σ / S, and LOQ = 10 * σ / S. The calculated values of LOD, LOQ, and the relative standard deviation (RSD), using the σ of the response (Yao et al., 2019), are listed in Table 5. The method shows good repeatability of less than 2 % (n = 4). Moreover, the calculated limits of detection were 0.086 nM 0.175 nM, 0.246 nM and 0.383 nM and the limit of quantification to be 0.287 nM, 0.585 nM, 0.821 nM and 1.278 nM corresponding to $Cd^{2+}$, $Pb^{2+}$, $Cu^{2+}$, and $Hg^{2+}$ ions, respectively.

In addition, the comparison of the modified electrode developed in this work, with other different modified electrodes from the literature, is listed in Table 6. This obtained result confirmed the applicability of the p-Tyr-BC-CPE electrode for the simultaneous detection of HMs ions.

### *5.2. Specificity, stability, and reproducibility of the p-Tyr-BC-CPE sensor*

One of the most important parameters for a valuable sensor is selectivity**.** To evaluate the interference of some metal ions that might be found in the environmental sample, the SWV technique was carried out under optimized conditions. Different ions such as $Co^{2+}$, $Fe^{2+}$, $Mg^{2+}$, $Mn^{2+}$, $Ni^{2+}$, $Zn^{2+}$ and $Ca^{3+}$ with a concentration ratio of 100:1 were added to the mixture of $Cd^{2+}$, $Pb^{2+}$, $Cu^{2+}$ and $Hg^{2+}$. The obtained solution was investigated in ABS supporting electrolyte (0.1 M, pH 5.5). The displayed results in Fig. 10a, show no significant changes were observed in the stripping peak currents intensity in the absence and presence of the interference ions. The changes in peak currents, compared to the blank, are less than 5 %, as listed in Table 7, and hence this influence is negligible. Thus, the modified electrode has high selectivity for simultaneous detection of the four target heavy metals.

The stability of the electrode prepared was also examined for a solution comprising mixed of $Pb^{2+}$, $Cd^{2+}$, $Cu^{2+}$, and $Hg^{2+}$ ions, by monitoring its current response every 10 days for 2 months. The maximum reduction of the peak current values obtained were 1.61 %, 3.53 %, 5.52 %, and 2.39 %, respectively, for these metal ions compared with their initial value, as presented in Fig. 10b. All measurements of the electrode modified with p-Tyr-BC showed excellent stability over this period.

Furthermore, the reproducibility of the p-Tyr-BC-CPE was tested by preparing 5 different modified electrodes and checked under the same procedure based on RSD = 100 * σ / $I_m$ (Guo et al., 2017). The current response by the 5 electrodes almost overlapped with relative standard deviations (RSDs) of 1.97 %, 1.72 %, 4.56 %, and 4.45 % for $Cd^{2+}$, $Pb^{2+}$, $Cu^{2+}$, and $Hg^{2+}$, respectively, as shown in Fig. 11c. These results of RSDs less than 5 % indicate that the modified electrode had excellent reproducibility.

Heavy metal ions can bind to amino acids due to their electron-rich functional groups such as COO–, $NH_2$, or

**Table 6** Comparison of various modified electrodes with the p-Tyr-BC-CPE.

| Modified Electrodes | Methods | Detection Limit (nM) | | | | References |
|---|---|---|---|---|---|---|
| | | Cd(II) | Pb(II) | Cu(II) | Hg(II) | |
| poly-Tyrosine/Bi/GCE | SWVSV | 0.12 | – | – | - | (Lin et al., 2021) |
| pg-$C_3N_4$ /$CoMn_2O_4$-GCE | SWASV | 21 | 14 | – | - | (Wang et al., 2021) |
| CPE-EDTA | SWV | – | 2.33 | – | - | (Laghlimi et al., 2021) |
| SPE/SWCNHs/BiF | SWVSV | 200 | 400 | – | - | (Wong et al., 2020) |
| ND-BC-CTS/GCE | SWVSV | 470 | 530 | – | - | (Han et al., 2020) |
| $COF_{BTLP-1}$/3D-KSC | DPSV | 12.3 | 11.8 | 18.6 | 21.4 | (Lu et al., 2019) |
| $GA_s$/UiO-66-$NH_2$-GCE | DPSV | 9.0 | 1.0 | 8.0 | 0.9 | (Xiao et al., 2014) |
| p-Tyr-BC-CPE | SWV | 0.0861 | 0.1754 | 0.2463 | 0.3834 | *This work* |

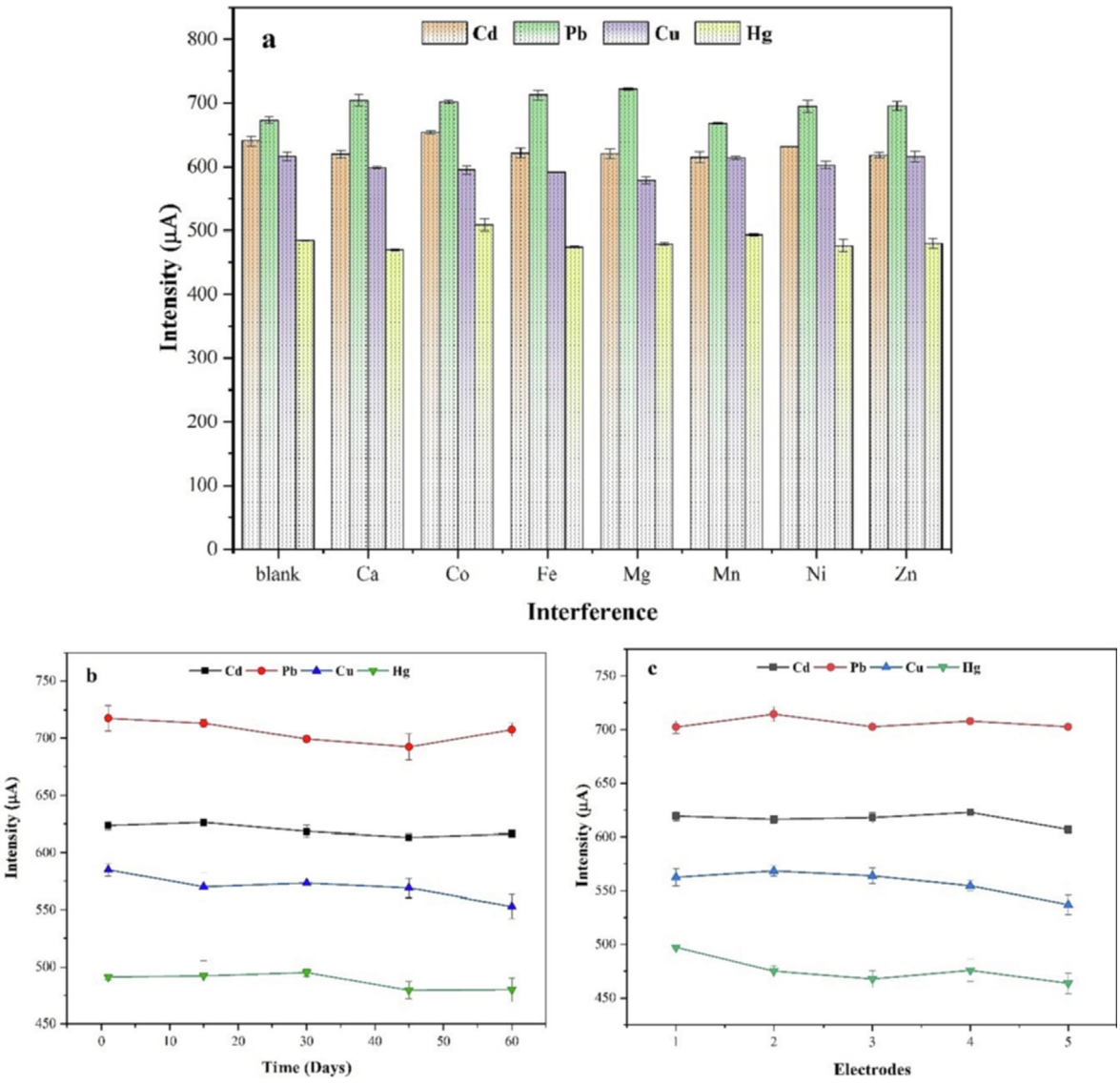


**Fig. 10** Interference (a), stability (b), and reproducibility (c) study.

**Table 7** Interference of some metal ions in the determination of Cd(II), Pb(II), Cu(II), and Hg(II) on p-Tyr-BC-CPE.

| Changes in peak currents (%) | | | | |
|---|---|---|---|---|
| Metal Ions | Cd(II) | Pb(II) | Cu(II) | Hg(II) |
| Ca(III) | 3.2206 | 4.6878 | 2.7096 | 3.1236 |
| Co(II) | 2.1207 | 4.3209 | 3.3121 | 4.9638 |
| Fe(II) | 2.9663 | 4.3310 | 3.9321 | 2.2147 |
| Mg(II) | 3.1470 | 4.2966 | 2.9036 | 1.1925 |
| Mn(II) | 4.0358 | 2.3609 | 0.3645 | 1.8759 |
| Ni(II) | 1.2552 | 3.2327 | 2.1252 | 1.7878 |
| Zn(II) | 3.4955 | 3.3559 | 0.4749 | 1.0172 |

through chelating interactions between the aromatic ring and the cation. Tyrosine is an exemplary amino acid that interacts with heavy metal ions in monomer form, or as part of a peptide or a protein. the p-Tyr membrane can promote the enrichment of $HM^{2+}$ on the surface of the carbonaceous electrodes. By complexation the surface of the electrode is enriched in

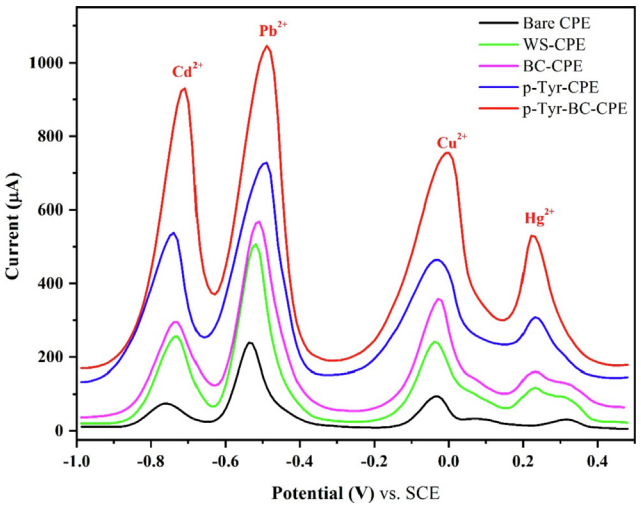


**Fig. 11** Square wave voltammograms of 0.1 mM Cd(II), Pb(II), Cu(II), and Hg(II) in 0.1 M ABS (pH 4.5) on the PCE, WS-CPE, BC-CPE, p-Tyr-CPE, and p-Tyr-BC-CPE, (all potentials in reference to the SCE).

heavy metals, and, by proximity, the ions can be sensed instantaneously. The effect of the biochar has two aspects: i) morphological: the thermal modification of WS results in an unorganized, porous structure. ii) chemical: the oxidation applied in parallel with the heating results in oxygen- and/or nitrogen-containing functional groups. These results validate the good selectivity, stability, and reproducibility of the p-Tyr-BC-CPE electrode hence the possibility for real trial analysis of the simultaneous determination of $Cd^{2+}$, $Pb^{2+}$, $Cu^{2+}$, and $Hg^{2+}$.

### *5.3. Performance of the p-Tyro-BC-CPE electrode in real samples*

To evaluate the applicability of the proposed electrode, the p-Tyr-BC-CPE was applied to the determination of $Cd^{2+}$, $Pb^{2+}$, $Cu^{2+}$, and $Hg^{2+}$ concentrations in real water and soil samples by SWV under the optimal experimental conditions. A standard addition method was deployed at 4 concentrations to obtain the analytical results in the 0.0–100.0 nM range (Nguyen et al., 2021). The results are summarized in Table 8, indicating acceptable recovery values ranging from 96.4 to 107.9 %. These results suggest the applicability of the electrode in the determination of HMs ions in real water and soil samples.

## 6. Practical applications of the sensor platform

Square wave voltammetry was used to detect heavy metal ions in a comparative response of various modified electrodes. Fig. 11 exemplifies the SWV analytical characteristics of the bare CPE, WS-CPE, BC-CPE, p-Tyr-CPE, and p-Tyr-BC-CPE to detect the presence of 0.1 mM of $Cd^{2+}$, $Pb^{2+}$, $Cu^{2+}$, and $Hg^{2+}$ in 0.1 M ABS with a potential range from −1.1 V to 0.5 V. Four stripping peaks were obtained with apparent current intensity, corresponding to the oxidation of $Cd^{2+}$, $Pb^{2+}$, $Cu^{2+}$, and $Hg^{2+}$ reduced on the surface of different electrodes studied, indicating that the simultaneous determination of these heavy metal ions is feasible. The comparison of these responses shows that the least intense peaks were obtained with the bare CPE. Indeed, the carbon paste is characterized by a less active surface due to the low conductivity of graphite.

However, the addition of walnut shell powder increased the sensitivity of the WS-CPE electrode. With the presence of biochar, even sharper stripping peaks could be obtained for $Cd^{2+}$, $Pb^{2+}$ $Cu^{2+}$, and $Hg^{2+}$, probably due to the enlarged electroactive surface area and the better adsorption capacity of BC-CPE (Leftheriotis et al., 2007). The carbon paste electrode modified with tyrosine film showed a higher peak current which indicates that the L-Tyrosine film can accumulate the metal ions. This indicates the good electro-catalytic activity of the electrode. For the p-Tyr-BC electrode, the clear and high peak currents demonstrate that it combines the advantages of tyrosine film and walnut shell biochar probably due to the combination of enlarged electrochemical active surface area, strong adsorption capability, and the specific complexing

**Table 8** Recovery of p-Tyr-BC-CPE in water and soil samples from the Bouregrag river.

| Metals | Added (μM) | Water | | Soil | |
|---|---|---|---|---|---|
| | | **Measured (μM)** | **Recovery (%)** | **Measured (μM)** | **Recovery (%)** |
| Cd(II) | 0.0 | 0.00075 | – | – | – |
| | 0.01 | 0.01079 | 107.9 | 0.00986 | 98.6 |
| | 0.1 | 0.1007 | 100.7 | 0.0992 | 99.2 |
| Pb(II) | 0.0 | 0.00048 | – | 0.00126 | – |
| | 0.01 | 0.01022 | 102.2 | 0.01048 | 104.8 |
| | 0.1 | 0.1064 | 106.4 | 0.10149 | 101.5 |
| Cu(II) | 0 | 0.00096 | – | 0.00244 | – |
| | 0.01 | 0.00998 | 99.8 | 0.00964 | 96.4 |
| | 0.1 | 0.0969 | 96.9 | 0.1017 | 101.7 |
| Hg(II) | 0.0 | 0.00028 | – | – | – |
| | 0.01 | 0.01012 | 101.2 | 0.01064 | 106.4 |
| | 0.1 | 0.1018 | 101.8 | 0.1048 | 104.8 |

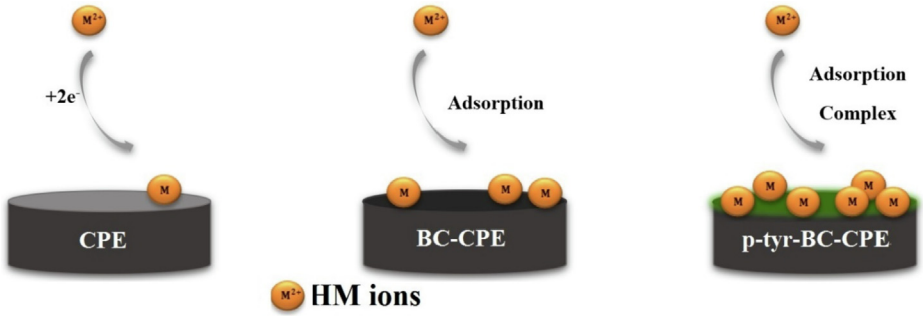


**Fig. 12** Schematic illustration of a mechanism for simultaneous detection of Cd(II), Pb(II) Cu(II) and Hg(II) by p-Tyr-BC.

ability of the p-Tyr-WS-BC platform (Fig. 12). This result confirms that the tyrosine-biochar electrode has promising properties for the simultaneous determination of heavy metal ions.

The possible electrochemical mechanisms for the detection of heavy metal ions can be defined in three phases. Metal ions were firstly accumulated on the surface of the modified electrode by adsorption, probably due to the binding by electrostatic attraction in the L-Tyr-BC platform. Subsequently, the heavy metal ions were preconcentrated at the modified electrode through an electrochemically reduced from a valence state of ($Fe^{2+}$) to ($Fe^{0}$) to enhance the mass transfer rate. Finally, these HMs ions are dissociated and turned back into the analytical solution and will be registered by the SWV technique [67].

These three phases of electrochemical mechanism can be expressed as follows:

$HMs(II)_{Solution}$ + p-Tyr-BC-CPE $_{Surface}$ → HMs(II)-p-Tyr-BC-CPE $_{Adsorption}$ (Accumulation).

$HMs(^{2+})$-p-Tyr-BC-$CPE_{Adsorption}$ + $2e^{-}$→$HMs(^{0})$-p-Tyr-BC-$CPE_{Surface}$ (Preconcentration/reduction).

$HMs(^{0})$-p-Tyr-BC-$CPE_{Surface}$- $2e^{-}$→$HMs(^{2+})_{Solution}$ + p-Tyr-BC-$CPE_{Surface}$ (Stripping/oxidation).

## 7. Conclusions

- The physicochemical characteristic results indicate that the obtained WS-BC is having a porous structure with the presence of hydroxyl functional groups that can be used as free positions and constitute the target sites.
- An innovative enhanced sensing platform based on the WS-BC, p-Tyr-BC modified CPE platform was developed. The combination of p-Tyr and WS-BC can deliver an excellent electrochemical platform for the detection of heavy metal ions. Effectively, after the fabrication of the tyrosine layer, the electrode performs well over what one would expect from the simple combination of BC- and p-Tyr modified CPE electrodes, therefore it is strongly assumed that not only a layer of p-Tyr but many –OH and –COOH groups were introduced to the surface of the platform electrode.
- The developed p-Tyr-WS-BC electrode was used to simultaneously detect $Cd^{2+}$, $Pb^{2+}$, $Cu^{2+}$, and $Hg^{2+}$ ions in water and soil samples. The limits of detection for $Cd^{2+}$, $Pb^{2+}$, $Cu^{2+}$, and $Hg^{2+}$ are much lower than the guideline values given by the world health organization (WHO).

## Declaration of Competing Interest

The authors declare that they have no known competing financial interests or personal relationships that could have appeared to influence the work reported in this paper.

## Acknowledgments

The authors acknowledge the support from the Moroccan Department of Higher Education and Scientific Research (DHESR) and the Hungarian National Research, Development and Innovation Office (NRDIO) bilateral scientific and technological cooperation agreement (Award No. 2018-2.1.10 -TÉT-MC-2018-00014).

## Research-data-availability for this article

The raw data of this manuscript is part of Youssra El Hamdouni's Ph.D. dissertation and will not be available.

## References

Ahmad, M., Rajapaksha, A.U., Lim, J.E., Zhang, M., Bolan, D.M., Vithanage, M., Lee, S.S., Ok, S.Y., 2014. Biochar as a sorbent for contaminant management in soil and water: a review. Chemosphere 99, 19–33. https://doi.org/10.1016/j.chemosphere.2013.10.071.

Albatrni, H., Qiblawey, H., Al-Marri, M.J., 2022. Walnut shell based adsorbents: A review study on preparation, mechanism, and application. J. Water Process Eng. 45,. https://doi.org/10.1016/j.jwpe.2021.102527 102527.

N. Baig, M. Sajid, "Applications of layered double hydroxides based electrochemical sensors for determination of environmental pollutants: A review," *Trends in Environmental Analytical Chemistry*, vol. 16, no. September. Elsevier, pp. 1–15, 2017, doi: 10.1016/j.teac.2017.10.003

Bandara, T., Franks, A., Xu, J., Bolan, N., Wang, H., Tang, C., 2020. Chemical and biological immobilization mechanisms of potentially toxic elements in biochar-amended soils. Crit. Rev. Environ. Sci. Technol. 50, 903–978. https://doi.org/10.1080/10643389.2019.1642832.

Bazargan, A., Rough, S.L., McKay, G., 2014. Compaction of palm kernel shell biochars for application as solid fuel. Biomass Bioenergy 70, 489–497. https://doi.org/10.1016/j.biombioe.2014.08.015.

P. Chakraborty, S. D. Singh, I. Gorai, D. Singh, W. U. Rahman, G. Halder, "Explication of physically and chemically treated date stone biochar for the sorptive remotion of ibuprofen from aqueous solution," *J. Water Process Eng.*, 33, no. October 2019, p. 101022, 2020, DOI: 10.1016/j.jwpe.2019.101022.

de Oliveira, P.R., Kalinke, C., Gogola, J.L., Mangrich, A.S., Junior, L. H.M., Bergamini, M.F., 2017. The use of activated biochar for development of a sensitive electrochemical sensor for determination of methyl parathion. J. Electroanal. Chem. 799, 602–608. https://doi.org/10.1016/j.jelechem.2017.06.020.

Duan, X., Zhang, C., Srinivasakannan, C., Wang, X., 2017. "Waste walnut shell valorization to iron-loaded biochar and its application to arsenic removal. Resour.-Effic. Technol. 3 (1), 29–36. https://doi.org/10.1016/j.reffit.2017.01.001.

Dudek, M., Adamczyk, B., Sitarz, M., Śliwa, M., Lach, R., Skrzypkiewicz, M., Raźniak, A., Ziąbka, M., Zuwała, J., Grzywacz, P., 2018. The usefulness of walnut shells as waste biomass fuels indirect carbon solid oxide fuel cells. Biomass Bioenergy 119, 144–154. https://doi.org/10.1016/j.biombioe.2018.09.026.

L. Farzin, M. Shamsipur, S. Sheibani, "A review: Aptamer-based analytical strategies using the nanomaterials for environmental and human monitoring of toxic heavy metals," *Talanta*, 174, no. May. Elsevier B.V., pp. 619–627, 2017, doi: 10.1016/j.talanta.2017.06.066.

A. Garciá-Miranda Ferrari, P. Carrington, S. J. Rowley-Neale, C. E. Banks, *Recent advances in portable heavy metal electrochemical sensing platforms*, 6, 10, 2020

M. B. Gumpu, S. Sethuraman, U. M. Krishnan, J. B. B. Rayappan, "A review on detection of heavy metal ions in water - An electrochemical approach," *Sensors and Actuators, B: Chemical*, 213. Elsevier B.V., pp. 515–533, 2015, doi: 10.1016/j.snb.2015.02.122.

Guo, Z., Li, D., Luo, X., Li, Y., Zhao, Q., Mengmeng, L., Zhao, Y., Sun, T., Ma, C., 2017. Simultaneous determination of trace Cd(II), Pb(II) and Cu(II) by differential pulse anodic stripping voltammetry using a reduced graphene oxide-chitosan/poly-l-lysine nanocomposite modified glassy carbon electrode. J. Colloid Interface Sci. 490, 11–22. https://doi.org/10.1016/j.jcis.2016.11.006.

Guo, X., Peng, Y., Li, N., Tian, Y., Dai, L., Wu, Y., Huang, Y., 2022. Effect of biochar-derived DOM on the interaction between Cu(II) and biochar prepared at different pyrolysis temperatures. J. Hazard. Mater. 421,. https://doi.org/10.1016/j.jhazmat.2021.126739 126739.

Gupta, S., Gupta, G.K., Mondal, M.K., 2019. Slow pyrolysis of a chemically treated walnut shell for valuable products: effect of process parameters and in-depth product analysis. Energy 181, 665–676. https://doi.org/10.1016/j.energy.2019.05.214.

Han, J., Yu, J., Guo, Y., Wang, L., Song, Y., 2020. "COFBTLP-1/three-dimensional macroporous carbon electrode for simultaneous electrochemical detection of Cd2+, Pb2+, Cu2+ and Hg2+". Sensors Actuators B Chem. 321,. https://doi.org/10.1016/j.snb.2020.128498 128498.

He, Z.L., Yang, X.E., Stoffella, P.J., 2005. Trace elements in agroecosystems and impacts on the environment. J. Trace Elem. Med Biol. 19 (2–3), 125–140. https://doi.org/10.1016/j.jtemb.2005.02.010.

Ifguis, O., Bouhdadi, R., Ziat, Y., George, B., Mbarki, M., 2022. Characterization and analysis of *Argania spinosa* shells from soussmassa area: application in the adsorption of Methylene Blue in aqueous solution. J. Nanomater. 2022, 6403838. https://doi.org/10.1155/2022/6403838.

Janu, R., Mrlik, V., Ribitsch, D., Hofman, J., Sedláček, P., Bielská, L., Soja, G., 2021. Biochar surface functional groups as affected by biomass feedstock, biochar composition, and pyrolysis temperature. Carbon Resour. Convers. 4, 36–46. https://doi.org/10.1016/j.crcon.2021.01.003.

Jlalia, I., Zouaoui, F., Chabbah, T., Chatti, S., Saint-Martin, P., Casabianca, H., Minot, S., Bessueille, F., Marestin, C., Mercier, R., Errachid, A., Abderrazak, H., Hammami, M., Jaffrezic-Renault, N., 2021. Adsorption characteristics of WFD heavy metal ions on new bio-sourced polyimide films determined by electrochemical impedance spectroscopy. J. Inorg. Organomet. Polym. 31, 2471–2482. https://doi.org/10.1007/s10904-020-01842-w.

C. Karakaş, D. Özçimen, B. İnan, "Potential use of olive stone biochar as a hydroponic growing medium," *J. Anal. Appl. Pyrolysis*, 125, no. December 2016, pp. 17–23, 2017, doi: 10.1016/j.jaap.2017.05.005.

Laghlimi, C., Ziat, Y., Moutcine, A., Hammi, M., Zarhri, Z., Maallah, R., Ifguis, O., Chtaini, A., 2020. Analysis of Pb (II), Cu (II), and Co (II) in drinking water by a new carbon paste electrode modified with an organic molecule. Chem. Data Collect. 29,. https://doi.org/10.1016/j.cdc.2020.100496 100496.

Laghlimi, C., Ziat, Y., Moutcine, A., Hammi, M., Zarhri, Z., Ifguis, O., Chtaini, A., 2021. A new sensor based on graphite carbon paste modified by an organic molecule for efficient determination of heavy metals in drinking water. Chem. Data Collect. https://doi.org/10.1016/j.cdc.2020.100595 100595.

Lateef, A., Nazir, R., Jamil, N., Alam, S., Shah, R., Khan, M.N., Saleem, M., Rehman, S., 2019. Synthesis and characterization of environmental friendly corncob biochar based nano-composite – a potential slow-release nano-fertilizer for sustainable agriculture. Environ. Nanotechnol., Monit. Manag. 11,. https://doi.org/10.1016/j.enmm.2019.100212 100212.

Leftheriotis, G., Papaefthimiou, S., Yianoulis, P., 2007. Dependence of the estimated diffusion coefficient of LixWO3 films on the scan rate of cyclic voltammetry experiments. Solid State Ionics 178 (3–4), 259–263. https://doi.org/10.1016/j.ssi.2006.12.019.

Li, X., Wang, C., Zhang, J., Liu, J., Liu, B., Chen, G., 2020. Preparation and application of magnetic biochar in water treatment: a critical review. Sci. Total Environ. 711,. https://doi.org/10.1016/j.scitotenv.2019.134847 134847.

Li, Y., Zhou, J., Song, J., Liang, X., Zhang, Z., Men, D., Wang, D., Zhang, X., 2019. Chemical nature of electrochemical activation of carbon electrodes. Biosens. Bioelectron. 144, (44). https://doi.org/10.1016/j.bios.2019.111534 111534.

Licursi, D., Antonetti, C., Fulignati, S., Vitolo, S., Puccini, M., Ribechini, E., Bernazzani, L., Galletti, A.M.R., 2017. "In-depth characterization of valuable char obtained from hydrothermal conversion of hazelnut shells to levulinic acid". Bioresour. Technol. 244 (Part 1), 880–888. https://doi.org/10.1016/j.biortech.2017.08.012.

J. Y. Lim, N. M. Mubarak, E. C. Abdullah, S. Nizamuddin, M. Khalid, Inamuddin, "Recent trends in the synthesis of graphene and graphene oxide based nanomaterials for removal of heavy metals — A review," *Journal of Industrial and Engineering Chemistry*, 66. The Korean Society of Industrial and Engineering Chemistry, pp. 29–44, 2018, DOI: 10.1016/j.jiec.2018.05.028.

Lin, W.F., Zhai, W.Y., Yan, Y., Liu, Y.Q., 2021. Highly sensitive Pb2+ sensor based on rod-like poly-tyrosine/Bi modified glassy carbon electrode combined with electrodeposition to eliminate Cu2+ interference. Microchem. J. 160,. https://doi.org/10.1016/j.microc.2020.105664 105664.

Loaiza, O.A., Lamas-Ardisana, P.J., Jubete, E., Ochoteco, E., Loinaz, I., Cabañero, G., García, I., Penadés, S., 2011. Nanostructured disposable impedimetric sensors as tools for specific biomolecular interactions: sensitive recognition of concanavalin A. Anal. Chem. 83 (8), 2987–2995. https://doi.org/10.1021/ac103108m.

Lu, M., Deng, Y., Luo, Y., Lv, J., Li, T., Xu, J., Chen, S.-W., Wang, J., 2019. Graphene aerogel-metal-organic framework-based electrochemical method for simultaneous detection of multiple heavy-metal ions. Anal. Chem. 91 (1), 888–895. https://doi.org/10.1021/acs.analchem.8b03764.

M. M. Foroughi, S. Jahani, M. Rajaei, Facile Fabrication of 3D Dandelion-Like Cobalt Oxide Nanoflowers and Its Functionalization in the First Electrochemical Sensing of Oxymorphone: Evaluation of Kinetic Parameters at the Surface Electrode, *J. Electrochem. Soc.* 166 B1300, https://doi.org/10.1149/2.0511914jes.

Madzaki, H., Karimghani, W.A.W.A.B., Nurzalikharebitanim, A., 2016. Carbon dioxide adsorption on sawdust biochar. Procedia Eng. 148, 718–725. https://doi.org/10.1016/j.proeng.2016.06.591.

J. Mehta *et al.*, "Progress in the biosensing techniques for trace-level heavy metals," *Biotechnology Advances*, 34, 1, Elsevier Inc., pp. 47–60, 2016, DOI: 10.1016/j.biotechadv.2015.12.001.

Moutcine, A., Laghlimi, C., Ziat, Y., Smaini, M.A., El Qouatli, S.E., Hammi, M., Chtaini, A., 2020. Preparation, characterization, and simultaneous electrochemical detection toward Cd (II) and Hg (II) of a phosphate/zinc oxide modified carbon paste electrode. Inorg. Chem. Commun., 107911 https://doi.org/10.1016/j.inoche.2020.107911.

M. B. Nguyen, D. T. N. Nga, V. T. Thu, B. Piro, T. N. P. Truong, P. T. H. Yen, . . . V. T. T. Ha,*"Novel nanoscale Yb-MOF used as highly efficient electrode for simultaneous detection of heavy metal ions*", Journal of Materials Science, 56(13), pp. 8172–8185, 2021, doi:10.1007/s10853-021-05815-3.

Nguyen, V., Nguyen, T., Chen, C., Hung, C., 2019. Influence of pyrolysis temperature on polycyclic aromatic hydrocarbons production and tetracycline adsorption behavior of biochar derived from spent coffee ground. Bioresour. Technol. 284, 197–203. https://doi.org/10.1016/j.biortech.2019.03.096.

Pamuk, D., Taşdemir, I.H., Ece, A., Canel, E., Kiliç, E., 2013. Redox pathways of aliskiren based on experimental and computational approach and its voltammetric determination. J. Braz. Chem. Soc. 24 (8), 1276–1286. https://doi.org/10.5935/0103-5053.20130162.

Popoola, L.T., 2019. Nano-magnetic walnut shell-rice husk for Cd(II) sorption: design and optimization using artificial intelligence and design expert. Heliyon 5 (8), e02381.

Qiu, M., Liu, L., Ling, Q., Cai, Y., Yu, S., Wang, S., Fu, D., Hu, B., Wang, X., 2022. Biochar for the removal of contaminants from soil and water: a review. Biochar 4, 19. https://doi.org/10.1007/s42773-022-00146-1.

R. Rapini, G. Marrazza, "Electrochemical apta-sensors for contaminants detection in food and environment: Recent advances," *Bioelectrochemistry*, 118. Elsevier B.V., pp. 47–61, 2017, doi: 10.1016/j.bioelechem.2017.07.004.

Salajegheh, M., Ansari, M., Foroghi, M.M., Kazemipour, M., 2019. Computational design as a green approach for facile preparation of molecularly imprinted polyarginine-sodium alginate-multiwalled carbon nanotubes composite film on glassy carbon electrode for theophylline sensing. J. Pharm. Biomed. Anal. 162, 215–224. https://doi.org/10.1016/j.jpba.2018.09.032.

Salih, F.E., Ouarzane, A., El Rhazi, M., 2017. Electrochemical detection of lead (II) at bismuth/Poly(1,8-diaminonaphthalene) modified carbon paste electrode. Arab. J. Chem. 10 (5), 596–603. https://doi.org/10.1016/j.arabjc.2015.08.021.

Senneca, O., Cerciello, F., Heuer, S., Ammendola, P., 2018. Slow pyrolysis of walnut shells in nitrogen and carbon dioxide. Fuel 225, 419–425. https://doi.org/10.1016/j.fuel.2018.03.094.

Sharma, N., Kaur, P., Jain, D., Bhullar, M.S., 2020. In-vitro evaluation of rice straw biochars' effect on bispyribac-sodium dissipation and microbial activity in soil. Ecotoxicol. Environ. Saf. 191,. https://doi.org/10.1016/j.ecoenv.2020.110204 110204.

Shivappa Adarakatti, P., Foster, C.W., Banks, C.E., Arun, A.K., Malingappa, P., 2017. Calixarene bulk modified screen-printed electrodes (SPCCEs) as a one-shot disposable sensor for the simultaneous detection of lead(II), copper(II) and mercury(II) ions: application to environmental samples. Sensors Actuators, A Phys. 267, 517–525. https://doi.org/10.1016/j.sna.2017.10.059.

M. A. Smaini, I. Smaini, M. Ennachete, C. Laghlimi, H. Saâdane, A. Moutcine, A. Chtaini Electrochemical determination of adenosine by natural phosphate modified carbon paste electrode: analytical application in serum, Sens Biosensing Res, 23 (2019), Article 100272, https://doi.org/10.1016/j.sbsr.2019.100272.

Tesfaye, G., Hailu, T., Ele, E., Negash, N., Tessema, M., 2021. Square wave voltammetric determination of quercetin in wine and fruit juice samples at poly (safranine O) modified glassy carbon electrode. Sens. Bio-Sensing Res. 34,. https://doi.org/10.1016/j.sbsr.2021.100466 100466.

F. R. Vieira, C. M. Romero Luna, G. L. A. F. Arce, I. Ávila, "Optimization of slow pyrolysis process parameters using a fixed bed reactor for biochar yield from rice husk," *Biomass and Bioenergy*, 132, 2020, DOI: 10.1016/j.biombioe.2019.105412.

Wang, Z., Liu, E., Zhao, X., 2011. Glassy carbon electrode modified by conductive polyaniline coating for determination of trace lead and cadmium ions in acetate buffer solution. Thin Solid Films 519 (15), 5285–5289. https://doi.org/10.1016/j.tsf.2011.01.176.

Wang, Y., Nie, Z., Li, X., Zhao, Y., Wang, H., 2021. Highly sensitive and selective electrochemical sensor based on porous graphitic carbon nitride/CoMn2O4 nanocomposite toward heavy metal ions. Sens. Actuators, B 346,. https://doi.org/10.1016/j.snb.2021.130539 130539.

Wang, Y.R., Zhai, W.Y., Liu, Y.Q., 2021. Study on Cd2+ determination using bud-like poly-L-Tyrosine/Bi composite film modified glassy carbon electrode combined with eliminating of Cu2+ interference by electrodeposition. Electroanalysis 33 (3), 744–754. https://doi.org/10.1002/elan.202060213.

Wong, A., Ferreira, P.A., Santos, A.M., Cincotto, F.H., Silva, R.A.B., Sotomayor, M.D.P.T., 2020. A new electrochemical sensor based on eco-friendly chemistry for the simultaneous determination of toxic trace elements. Microchem. J. 158,. https://doi.org/10.1016/j.microc.2020.105292 105292.

Wu, Q., Bi, H.M., Han, X.J., 2021. Research progress of electrochemical detection of heavy metal ions. Chinese J. Anal. Chem. 49 (3), 330–340. https://doi.org/10.1016/S1872-2040(21)60083-X.

Wu, L., Li, B., Liu, M., 2018. Influence of aromatic structure and substitution of carboxyl groups of aromatic acids on their sorption to biochars. Chemosphere 210, 239–246. https://doi.org/10.1016/j.chemosphere.2018.07.003.

Xiao, L., Xu, H., Zhou, S., Song, T., Wang, H., Li, S., Gan, W., Yuan, Q., 2014. Simultaneous detection of Cd(II) and Pb(II) by differential pulse anodic stripping voltammetry at a nitrogen-doped microporous carbon/Nafion/bismuth-film electrode. Electrochim. Acta 143, 143–151. https://doi.org/10.1016/j.electacta.2014.08.021.

Xiong, W., Zhang, P., Liu, S., Lv, Y., Zhang, D., 2021. Catalyst-free synthesis of phenolic-resin-based carbon nanospheres for simultaneous electrochemical detection of Cu (II) and Hg (II). Diam. Relat. Mater. 111,. https://doi.org/10.1016/j.diamond.2020.108170 108170.

Xu, X., Gao, J., Tian, Q., Zhai, X., Liu, Y., 2017. Walnut shell derived porous carbon for asymmetric all-solid-state supercapacitor. Appl. Surf. Sci. 411, 170–176. https://doi.org/10.1016/j.apsusc.2017.03.124.

V. B. Yadav, R. Gadi, S. Kalra, "Clay-based nanocomposites for removal of heavy metals from water: A review," *Journal of Environmental Management*, 232, no. July 2018. Elsevier, pp. 803–817, 2019, doi: 10.1016/j.jenvman.2018.11.120.

Yang, J., Qiu, K., 2010. Preparation of activated carbons from walnut shells via vacuum chemical activation and their application for methylene blue removal. Chem. Eng. J. 165 (1), 209–217. https://doi.org/10.1016/j.cej.2010.09.019.

Yang, L., Wang, L., Li, K., Ye, B., 2014. Sensitive voltammetric determination of neohesperidin dihydrochalcone based on SWNTs modified glassy carbon electrode. Anal. Methods 6 (23), 9410–9418. https://doi.org/10.1039/c4ay02004a.

Yao, Y., Wu, H., Ping, J., 2019. Simultaneous determination of Cd(II) and Pb(II) ions in honey and milk samples using a single-walled carbon nanohorns modified screen-printed electrochemical sensor. Food Chem. 274, 8–15. https://doi.org/10.1016/j.foodchem.2018.08.110.

Zbair, M., Ait Ahsaine, H., Anfar, Z., Slassi, A., 2019. Carbon microspheres derived from walnut shell: rapid and remarkable uptake of heavy metal ions, molecular computational study and surface modeling. Chemosphere 231, 140–150. https://doi.org/10.1016/j.chemosphere.2019.05.120.

J. Zhang, J. Shao, D. Huang, Y. Feng, X. Zhang, S. Zhang, H. Chen, "Influence of different precursors on the characteristic of nitrogen-enriched biochar and SO2 adsorption properties," *Chem. Eng. J.*, 385, no. December 2019, p. 123932, 2020, DOI: 10.1016/j.cej.2019.123932.

Zhang, X., Zhang, Y., Ngo, H.H., Guo, W., Wen, H., Zhang, D., Li, C., Qi, L., 2020. Characterization and sulfonamide antibiotics adsorption capacity of spent coffee grounds based biochar and hydro-char. Sci. Total Environ. 716. https://doi.org/10.1016/j.scitotenv.2020.137015.